Metallogenic setting and temporal evolution of porphyry Cu-Mo mineralization and alteration in the Delamerian Orogen, South Australia: Insights from zircon U-Pb, molybdenite Re-Os, and *in situ* white mica Rb-Sr geochronology

Wei Hong,[1,2,3,†,☼] Adrian Fabris,[2,3] Tom Wise,[2,3] Alan S. Collins,[1,3] Sarah Gilbert,[4] David Selby,[6] Stacey Curtis,[2,3,5,☼☼] and Anthony J. Reid[2,3]

[1] *Department of Earth Sciences, School of Physical Sciences, The University of Adelaide, Adelaide, SA 5005, Australia*

[2] *Geological Survey of South Australia (GSSA), Department for Energy and Mining, 11 Waymouth Street, Adelaide, SA 5001, Australia*

[3] *Mineral Exploration Cooperative Research Centre (MinEx CRC), Bentley, WA 6102, Australia*

[4] *Adelaide Microscopy, The University of Adelaide, Adelaide, SA 5005, Australia*

[5] *STEM, University of South Australia, Mawson Lakes, SA 5095, Australia*

[6] *Department of Earth Sciences, Durham University, Durham, United Kingdom DH1 3LE*

† Corresponding author: e-mail, wei.hong@utas.edu.au

☼ Present address: Centre for Ore Deposit and Earth Sciences (CODES), University of Tasmania, Private Bag 79, Hobart 7001, Australia

☼☼ Present address: Copper Search Limited, 557 Magil Road, Magil, SA 5072, Australia

Abstract

Paleozoic porphyry-style hydrothermal alteration and mineralization has previously been recognized within the Delamerian Orogen, South Australia, where porphyry prospects include Anabama Hill, Netley Hill, and Bendigo. However, limited exploration due in part to thick postmineralization cover hindered the understanding of the temporal context, metallogenic setting, and mineral potential of the porphyry systems along the Proterozoic continental margin of Australia. In this study, we have characterized the hydrothermal alteration and mineralization of these porphyry occurrences. Zircon U-Pb, molybdenite Re-Os, and white mica Rb-Sr ages have been determined to constrain the timing for emplacement of magmatic intrusions, precipitation of metal-bearing sulfides, and duration of hydrothermal alteration in the Delamerian Orogenic Belt. Zircon U-Pb LA-ICP-MS analyses of nine granitoids reveal that the intrusive rocks were emplaced mostly between 485 Ma and 465 Ma, whereas three intrusions at Bendigo have zircon U-Pb ages of 490 to 480 Ma. Molybdenite ID-NTIMS Re-Os dating of the four prospects identify two porphyry Cu-Mo mineralization events at 480 Ma and 470–460 Ma, respectively. Nineteen white mica Rb-Sr LA-ICP-MS/MS analyses return an age range between 455 Ma and 435 Ma for phyllic alteration at the Anabama Hill and Netley Hill prospects, whereas intensive white mica-quartz-pyrite alteration at Bendigo prospect appears to have developed between 470–460 Ma. These geochronologic results indicate that the Delamerian porphyry systems post-dated subduction-related magmatism in the region (514–490 Ma), but instead, formed within an inverted back arc regime, where mineralized magmas and fluids ascended along favorable lithospheric-scale structures, probably due to asthenospheric upwelling triggered by mafic delamination. Porphyritic stocks, dikes, and aplites with ages of 470–460 Ma are the most likely hosts to porphyry-style mineralization in the Delamerian Orogen that appear to have formed simultaneously with the oldest known porphyry systems in intraoceanic Macquarie Arc (e.g., Marsden, E43, and Milly Milly; 467 – 455 Ma). These results emphasize the significance and potential of Early-Middle Ordovician intrusive systems to host such a type of magmatic-hydrothermal mineralization in the Delamerian Orogen.

Introduction

The Delamerian Orogen in southeastern Australia has been regarded as a Proterozoic continental rift margin that evolved to a convergent Andean-style subduction-related continental margin in the Early Paleozoic (Preiss, 2000; Foster and Gray, 2000; Foden et al., 2002, 2006, 2020; Kemp, 2003; Kemp et al., 2009; Cayley, 2011). The orogen has experienced extensive deformation, metamorphism, and magmatism between the middle Cambrian and the early Ordovician, which is considered to have been driven by a collisional event that terminated subduction (Cayley, 2011). This terrane has considerable potential for formation of magmatic – hydrothermal mineral deposits, but has been poorly explored. Porphyry-style Cu-Mo mineralization in the Delamerian Orogen was first identified in the 1970s, and was considered as a possible third porphyry Cu-Mo mineralization cluster in Australia (Sinclair, 2007). Renewed interest in the region has followed the discovery of the Thursdays Gossan porphyry deposit in the adjacent Stavely Arc in Victoria, a high sulfidation-style Cu-Au deposit that is estimated to contain a mineral resource of 28.3 Mt at 0.75 % Cu and 0.11 g/t Au within a high-grade blanket overlying the porphyry stock (Stavely Minerals, 2022). However, no other economically significant deposits have been recognized in this Early Paleozoic magmatic arc, due in part to poor geological understanding and limited exploration of the Delamerian orogen mineral systems, which are largely buried beneath Cenozoic cover sequences of the Murray Basin (Fig. 1).

This study presents a reconnaissance investigation on the hydrothermal alteration and mineralization of several porphyry-style Cu-Mo prospects in the Delamerian Orogen, including Anabama Hill, Netley Hill, Bendigo, and Colebatch (Figs. 1–2). Zircon and molybdenite have been separated from intrusive rocks and sulfide-quartz veins for LA-ICP-MS U-Pb and ID-NTIMS Re-Os isotopic dating, respectively, as geochronology is crucial to refine metallogenic and genetic models for porphyry mineral systems in the region, and to determine the timing of ore mineral precipitation, elucidate the life span of a magmatic-hydrothermal mineralizing and alteration events, and to encourage and facilitate mineral exploration (Chiaradia et al., 2013; Pollard et al., 2021). Additionally, we utilized the recent development of LA-ICP-MS/MS systems for *in situ* Rb-Sr isotopic dating of white mica (Zack and Hogmalm, 2016; Hogmalm et al., 2017; Redaa et al., 2021, 2022; Subarkah et al., 2022). These new dates are presented to determine the timing and duration of magmatic-hydrothermal alteration associated with porphyry-style Cu-Mo mineralization, to provide a framework to

discuss the tectonomagmatic evolution, and to springboard mineral exploration in the Delamerian greenfield province.

Regional geology

The Tasmanides accretionary orogenic system occupies the eastern third of Australia and can be broadly split into four major orogens (Fig. 1A). From the west to east, these are the Delamerian Orogen (~520–490 Ma), Lachlan Orogen (485–340 Ma), Thomson Orogen (510–495 Ma) to the north, and New England Orogen (305–230 Ma; Foster and Gray, 2000; Foden et al., 2006; Kemp et al., 2009). Together the orogens represent the eastward progressive continental growth of a Pacific-facing margin directly postdating the Gondwana Supercontinent assembly (Foster and Gray, 2000; Collins, 2002; Cawood, 2005; Kemp et al., 2009; Foden et al., 2020; Merdith et al. 2021). The Delamerian Orogen is the oldest part of the Tasmanides and represents a middle Cambrian, west dipping Andean-style advancing subduction zone (Foden et al., 2006, 2020; Robertson et al., 2015) superimposed on a Neoproterozoic to Cambrian continental passive margin (the Adelaide Superbasin; Lloyd et al., 2020). The orogen is best exposed in South Australia, defined as the Adelaide Fold Belt which includes the Flinders Ranges to the north (including the Nackara Arc), Mount Lofty Ranges in the central region (Transitional Domain), and extending south to Fleurieu Peninsular and Kangaroo Island (Fig. 1B; Marshak and Flöttmann, 1996). The Delamerian Orogen continues eastwards for approximately 300 km from the Adelaide Hills to the Grampians-Stavely Belt in western Victoria (i.e., Stavely Arc; Fig. 1B), bounded by the Moyston and Stawell-Ararat fault systems that form the westmost margin of the Lachlan Orogen (Foster and Gray, 2000; Aivazpourporgou, 2013). The Stavely Arc comprises the Glenelg River Complex and the Mt Stavely Volcanic Complex. It is characterized by Cambrian mafic-ultramafic units (e.g., serpentinite), and basaltic, andesitic, and dacitic lavas that were deformed at ca. 495 Ma (Foster and Gray, 2000; Aivazpourporgou, 2013; Schofield, 2018; Bowman et al., 2019). To the northeast, this belt stretches into the western portion of New South Wales along the northeast margin of Paleoproterozoic-Mesoproterozoic Curnamona Craton, as the Loch Lilly-Kars Belt, Bancannia Trough, and Koonenberry Belt (Fig. 1B), which contain exposures of early to middle Cambrian volcano-sedimentary rocks deposited from 515 to 496 Ma (Greenfield et al., 2011; Johnson et al., 2016). Across Bass Strait in western Tasmania, Cambrian rocks are exposed in the Dundas Though and Mount Read Volcanic field and were deformed by the late Cambrian Tyennan Orogen (Seymour et al., 2007). This belt probably also connects with Northern Victoria Land in Antarctica (Foden et al., 2006).

The Adelaide Fold Belt contains deformed rocks of the Adelaide Superbasin (Lloyd et al., 2020). These consist mainly of the Neoproterozoic Adelaidean Supergroup as well as, in the region of interest for this study, the Cambrian Normanville Group and succeeding Kanmantoo Group of the Stansbury Basin (Fig. 1B). Sedimentation in the Adelaidean Superbasin initiated around 850 Ma due to rifting and extension related to the Rodinian breakup (Lloyd et al., 2022) and evolved into thick passive margin sequences overlying the Archean-Proterozoic South Australian Craton (Preiss, 2000; Lloyd et al., 2020). The Adelaidean Supergroup can be further classified into at least four volcano-sedimentary groups, i.e., the Callanna (ca. 850–790 Ma), Burra (ca. 790–730 Ma), Umberatana (ca. 730–640 Ma), and Wilpena Groups (ca. 640–541 Ma). The Cambrian Normanville Group is a sedimentary succession of limestone, siltstone, shale, and minor calcareous sandstone, marking an upward transition from a shallow nearshore to deep-water environment (Betts et al., 2018). Zircons from a thin tuff unit in the upper Heatherdale Shale of this group yield a weighted mean CA-TIMS age of 515 ± 0.6 Ma (Betts et al., 2018). The Kanmantoo Group is dominated by extensive deep marine turbiditic sequences of sandstone, mudstone, black shale, and limestone that unconformably overlie the Normanville Group in southern South Australia (Jago et al., 2003; Haines et al., 2009; Betts et al., 2018). The foliated Rathjen Gneiss granite intruded the Kanmantoo Group and has a SHRIMP zircon crystallization age of 514 ± 4 Ma (Foden et al., 1999), providing a minimum age for the deposition of the Kanmantoo Group. The central part of this orogenic belt is largely concealed by cover sequences with thickness up to 1.5 km that define the Cretaceous to Cenozoic Otway and Murray Basins, with sporadic outcrops of Neoproterozoic-Cambrian rocks in western Victoria and New South Wales (Fig. 1B).

The Adelaide Fold Belt experienced three phases of deformation in the Middle to Late Cambrian (i.e., the Delamerian Orogeny, 514–490 Ma; Foden et al., 2006). In Victoria, the broadly coeval Staveley Arc preserves four deformation stages (Schofield, 2018). The early D1 fold and thrust deformation is interpreted to have occurred after ca. 514 Ma, and is thought to have concluded the deposition of the Kanmantoo Group (Foden et al., 2006, 2020; Betts et al., 2018). This deformation event was succeeded by D2 (510 ± 2 Ma) and D3 upright folding episodes that may have continued to 490 ± 5 Ma (Flöttmann et al., 1998; Foden et al., 2006). These episodes of deformation are interpreted to be a consequence of initial subduction of the oceanic crust of the Pacific basin. They imbricated and thickened rocks of the Adelaide Superbasin during volcanic arc formation, leading to concurrent low P–high T metamorphism and magmatism (Flöttmann et al., 1998; Foden et al., 2006, 2020; Betts et al., 2018). Middle to Late Cambrian (ca. 520–500 Ma) tholeiitic basalt sills and dikes intruded

the Kanmantoo Group, and coeval tholeiitic mafic-ultramafic rocks have been reported from the Stavely Arc of Victoria and Mt Wright Arc (Koonenberry Belt) of New South Wales. They are interpreted to be rifting-related, back arc basalts sourced from a depleted mantle (Greenfield et al., 2011; Schofield, 2018; Foden et al., 2020). Numerous syn-tectonic I- and S-type granites intruded the central-south portion of the Adelaide Fold Belt from 514 to 490 Ma, and were followed by widespread 490–470 Ma A-type granites and co-magmatic mafic rocks (Turner et al., 1992; Foden et al., 1999, 2006, 2002). Post-tectonic A-type granitic magmatism marked the termination of the Delamerian Orogeny, with intense activities continuing for 25 ± 5 million years (m.y.), accompanied with buoyancy-controlled rapid uplift and exhumation (Alias et al., 2002; Foden et al., 2006, 2020). During this period, the Tasmanide accretion front shifted further eastward configuring the Lachlan Orogen (Foster and Gray, 2000; Kemp et al., 2009; Foden et al., 2006, 2020).

Delamerian porphyry Cu-Mo systems

Many mineral deposits and prospects have been discovered in the Delamerian Orogen of South Australia (Curtis, 2020), including metamorphosed sediment-hosted Cu-Au deposits (e.g., Kanmantoo; Pollock et al., 2018; Fig. 1B), volcanic-hosted massive sulfide mineralization (e.g., Sherlock; Rockwell Resources and Kelpie Exploration, 2017; Fig. 1B), SEDEX Zn-Pb-Ag deposits (Angas, Wheal Ellen, and Mount Torrens; Tott et al., 2019; Fig. 1B), and numerous vein-type gold mineralization (Griessmann, 2011). Porphyry and skarn Cu-Mo-Au prospects have also been discovered in this belt (Fig. 1B), including Anabama Hill, Blue Rose, Netley Hill, Bendigo, and Colebatch. This porphyry belt continues southeast towards the Victorian Stavely Arc (Thursday's Gossan and Junction prospects; Duncan et al., 2018; Stavely Minerals, 2022; Fig. 1B), where SHRIMP U-Pb zircon and Re-Os molybdenite ages (505–498 Ma; Duncan et al., 2018) implied that the Victorian porphyry systems are products of subduction-related magmatism during the Delamerian Orogeny. Whole-rock and zircon analyses from the Loch Lilly-Kars Belt in NSW (Fig. 1B) suggest that Devonian monzonite porphyries, as opposed to Cambrian intrusive rocks, have strong indicators of fertility with respect to porphyry Cu mineralization (Baatar et al., 2020). This implies that the mineralized porphyries at Loch Lilly-Kars (Fig. 1B) are likely a separate metallogenic event. Drill hole chips and hand specimens from Anabama Hill, Netley Hill, Bendigo, and Colebatch prospects in South Australia were sampled for geologic and chronologic investigations in this study. The sample lithology, coordinate, and drill hole details are included in Appendix Table A1.

Anabama Hill Cu-Mo prospect

The Anabama Hill prospect (Fig. 2A) was discovered in 1971 by geologic mapping, soil geochemistry, and induced polarization (IP) investigations, and subsequently tested with seven diamond drill holes (Morris, 1977; Rattigan et al., 1982). Best mineralized intercepts include 5 m at 0.1% Cu in drill hole ANDDH4 and 5.5 m at 0.1% Mo in drill hole ANDDH6 (Morris, 1977). Follow-up investigations revealed that Cu grade increased to 0.17 – 0.38% and Mo up to 620 ppm in the muscovite-rich altered zones (Rattigan et al., 1982). Granodiorite is the major component of the Anabama Granite. Minor phases include quartz diorite, monzogranite, dacite porphyry, and lamprophyre dikes. They emplaced into the Neoproterozoic Umberatana Group of mica schists, tillites, quartzites, and siltstones (Morris, 1977; Rattigan et al., 1982). The coarse-grained, equigranular granodiorite is mainly composed of plagioclase, K-feldspar, quartz, and biotite (Figs. 3A-B), with minor hornblende. The diorite occurs as intermittent dikes, with thicknesses from 0.5 to 45 m in the drill holes. It is dominated by plagioclase phenocrysts (up to 20%) up to 3 mm in diameter (Figs. 3B–C). Locally, granodiorite enclaves are enclosed within the plagioclase-phyric diorite (Fig. 3C). The monzogranite dike (10–20 cm wide) was mainly observed in drill hole DDHAN7, from 625 to 796 m, with a pale-reddish appearance (Fig. 3F). A reddish 10–50 cm wide K-feldspar-phyric dike intruded the granodiorite, and was intensively cut by multiple sets of pyrite-quartz-muscovite veins (1 –10 mm wide; Fig. 3E).

Potassic alteration is confined to an area delineated by drill holes DDHAN7, ANDDH3, and ANDDH2 (Fig. 2A; Table 1). Discontinuous K-feldspar-quartz veinlets (several mm in width; K1 vein) cut the diorite porphyry (Fig. 3D) and granodiorite, and occur below intensely developed muscovite alteration zone. Locally, granular K-feldspar veinlets (K2 vein) sealed fractures in the granodiorite and were reopened by epidote-chlorite veins (P1 vein). Plagioclase phenocrysts in the diorite were partially altered to albite, and weak to moderate muscovite-chlorite-epidote alteration overprinted the groundmass (Figs. 3B–D). Disseminated chalcopyrite and pyrite occur sporadically in the porphyritic dike, and are associated with potassic alteration (Figs. 3F and A1A).

Intermediate to strong epidote-chlorite alteration occurs as veinlets (< 1 cm), veins (1–5 cm), and thick veins (> 5 cm; Table 1) in drill holes DDHAN4 and DDHAN5 (Figs. 3E, 3G-H, and Fig. A1D). These veins are commonly represented by chlorite-epidote ± albite ± pyrite (P1 vein). A secondary type of propylitic veins is defined by epidote-quartz-magnetite-pyrite assemblages (P2 vein; Fig. A1C), cutting the monzogranite along contacts with the granodiorite (e.g., 163.5 m, AHDDH5). The P1 vein locally contains chalcopyrite and/or molybdenite disseminations, overprinted by pyrite-muscovite-quartz veins (e.g., Figs. 3E, 3H, and 7B).

Extensive pyrite-white mica[1]-quartz alteration (Figs. 3F-I) prevails in the granodiorite, diorite, and monzogranite, capped by a 50 m-thick weathering zone consisting of kaolinite, illite, montmorillonite, jarosite, and goethite. The phyllic zone at Anabama Hill extends intermittently downwards for > 700 m and occurs commonly as multiple veins and veinlets (Table 1), which define a semi-circular shaped dome with a diameter of 900 m. Green to dark muscovite-quartz ± pyrite veins (10 cm wide; W1 vein) commonly cut the monzogranite towards the base of the drill hole DDHAN7 (744 m; Fig. 3F), with disseminated molybdenite and chalcopyrite (Figs. 7C and A1B). The W1 vein is texturally comparable to pale-green white mica veins in the El Salvador (Chile), Butte (USA), and Highland Valley (British Columbia) porphyry Cu-Mo ± Au deposits, representing the transition between potassic-silicate and typical sericitic alterations (Seedorff et al., 2005; Alva-Jimenez et al., 2020). Another group of phyllic alteration are defined by white mica-quartz-magnetite-pyrite assemblages (W2 vein), with minor coarse-grained chalcopyrite (Fig. 3I). The most widespread phyllic vein is characterized by extensive quartz-pyrite veins (> 1 m wide) with thick white mica halos (W3 vein). Euhedral, coarse-grained molybdenite, pyrite, and muscovite with fine-grained chalcopyrite and bornite (e.g., Fig. A1E) typically occur along fractures or as discrete clots within the centerline quartz masses of the W3 veins, superimposed on the potassic and/or propylitic alteration assemblages (Figs. 3G-3I, A1F, and 7A).

Netley Hill Cu-Mo prospect

The Netley Hill prospect (Fig. 2B) is located ca. 30 km southwest of Anabama Hill, within a discrete intrusive body defined by aeromagnetic data (Fig. 1B and Table 1; Hosking, 1970; Clifford, 2008). Trace indications of mineralization, such as turquoise, quartz pegmatites, vein stockworks, and greisen breccias, are present at the surface (Fig. 2B; Hosking, 1970). Copper and Mo anomalies are associated with a massive muscovite-quartz ± pyrite alteration over 1.5 km long by 750 m wide. PacMag Metals Ltd targeted a 3 km long by 1 km wide IP chargeability anomaly in 2008. Four diamond drill holes (NTDD001 to NTDD004), each approximately 350 m in length, then identified low-grade Cu and Mo mineralization (350 m at 0.1% Cu, 0.015% Mo, and 1g/t Ag), with the highest grades of 0.6% Cu and 0.17% Mo in drill hole NTDD001 (Clifford, 2008).

[1] White micas in the Delamerian prospects range in composition from muscovite, paragonite to phengite using HyLogger™ spectral data by Geological Survey of South Australia, available via SARIG. For simplicity, muscovite is referred equivalently to white mica in the following text.

Drillings intersected granodiorite, porphyritic diorite, biotite-phyric granite, red K-feldspar granite, and minor aplite dikes (Fig. 4). The granodiorite is dominant at Netley Hill. The plagioclase-phyric diorite dikes cut the granodiorite and contain minor augite, quartz, and biotite (Fig. 4B). Abundant needle-like biotite phenocrysts occur in a red granitic stock that commonly associates with a red granitic stock (Fig. 4F), which consists of K-feldspar, biotite, albite, and quartz, with minor magnetite and apatite. A reddish fine-grained aplite dike of 20–30 cm in length has been cut by a molybdenite-pyrite ± chalcopyrite-quartz vein. Aplite-clast breccias were cemented locally by massive white mica, pyrite, albite, and quartz (Fig. 7D).

Potassic alteration has two categories of veins at Netley Hill (Figs. 4A-B; Table 1). Discontinuous quartz-biotite ± pyrite ± chalcopyrite veins (2–3 mm wide; Fig. A2A) with K-feldspar halos (1–2 cm wide) characterize the K1 vein, which are commonly presented in the granodiorite and granite (Fig. 4A). Pale K-feldspar veins with disseminated sulfides (K2 vein) occur in plagioclase-phyric diorite, where they were truncated by quartz-white mica-pyrite veins (1–5 cm wide; W1 vein), both which were reopened by elongated quartz-rich veins (2–10 cm wide) with a centerline of pyrite ± chalcopyrite (W3 vein; Fig. 4B). Chalcopyrite and bornite occur as disseminations, veins, and veinlets restricted to potassic alteration in drill holes of 180–340 m (Figs. 4D-4F).

Epidote-chlorite assemblage is not prevalent at Netley Hill (Table 1). Weak chlorite ± epidote-biotite alteration occurs intermittently in drill hole NTDD004, and was observed between 105–150 m and 310–340 m of drill hole NTDD003. The propylitic alteration resulted from selective replacement of preexisting plagioclase, augite, and/or biotite in the granitic hosts (Fig. A2B).

Abundant white mica-quartz-pyrite veins and stockworks characterize the phyllic alteration zone (Table 1) which extends from 50–300 m in depth, above a potassic alteration domain. The prevalent quartz-white mica-pyrite assemblage (W1 vein) typically reopened the preexisting K-feldspar veins, producing centerlines filled by 1–5 mm wide pyrite-chalcopyrite veinlets (Figs. 4C and 7F). The W1 veins are crosscut locally by flat quartz-pyrite veins and minor K-feldspar remnants occur on the margin of the white mica-quartz halos (Fig. 4C). White mica-quartz-magnetite-pyrite ± chalcopyrite defines W2 veins – they have a thin centerline of magnetite and pyrite enveloped by pale to greenish white mica and quartz (1–5 cm wide; Fig. 4D). Copper sulfides are disseminated in pervasive muscovite-pyrite-quartz veins (10–20 cm wide; W3 vein) that locally exceed 60% of the rock mass (cf. Fig. A2). Minor fine-grained molybdenite is present in thick, sheeted quartz ± pyrite-white mica-rich veins as observed at the base of drill hole NTDD001 (Fig. 4G). The phyllic alteration zone at Netley

Hill is blanketed by an argillic alteration domain that occurs from the surface down to 35–120 m. The argillic assemblages consist of kaolinite-muscovite-jarosite ± montmorillonite ± dickite and locally extend to a greater part and overprint the potassic zone along fractures and faults in the granitic intrusions.

Bendigo Cu-Mo prospect

The Bendigo prospect is located ca. 100 km southwest of the Anabama Hill and Netley Hill systems, within the east flank of the Bendigo Granite (Fig. 2C). Surface soil and IP survey identified three chargeability anomalies, which initiated the drilling of seven diamond cores (BD1 to BD7; 125 to 305 m deep) in this area (Fig. 2C; Langsford, 1971, 1973). Low Cu concentrations range from 20 to 80 ppm, with highest grades intersected by drill hole BD1 (3,100 ppm Cu over 11 m). Molybdenum concentrations are typically between 14 and 140 ppm, with a peak value of 1,100 ppm (Langsford, 1971). Historical investigation into the Cu-Mo porphyry potential of the Bendigo prospect identified relatively abundant quartz-muscovite veins cutting the granitic intrusions; however, sulfide mineralization was generally less than 0.5 % by volume and mainly consisted of pyrite, chalcopyrite, molybdenite, and minor bornite (Fig. 2C).

The Bendigo Granite intruded Neoproterozoic metasedimentary siltstones and sandstones (Umberatana Group) and formed dark grey to green, laminated hornfels halos at its margins. The main phase of this intrusion is a medium-grained, equigranular granodiorite, consisting of plagioclase, K-feldspar, quartz, biotite, and minor hornblende (Figs. 5A-B). Minor fine-grained, biotite-rich granodiorite variants are present and plagioclase-phyric dioritic dikes intruded the main granodiorite (Figs. 5F-H). A reddish, medium- to fine-grained granite, consisting of K-feldspar, quartz, biotite, and minor plagioclase and muscovite (Fig. 5I), has gradational contacts with the grey granodiorite.

Discontinuous K-feldspar-quartz ± biotite ± pyrite veins (K1 veins; Fig. A3A; Table 1) and thick quartz-pyrite ± molybdenite veins with K-feldspar halos (K2 veins) cut the medium-grained granodiorite (Fig. 5A). Plagioclase and K-feldspar have undergone selective epidote ± chlorite alteration. The plagioclase-phyric diorite dikes have been typically cut by thin biotite-quartz ± pyrite veinlets with K-feldspar envelops of 1-2 mm wide (K3 veins; Figs. 5F-G). Banded molybdenite-quartz-pyrite ± chalcopyrite veins range in width from 0.5–5 cm in the granodiorite and porphyritic diorite stocks (BMQ veins; Figs. 5B-5D, and 5H); locally, they are rimmed by 2–5 mm wide K-feldspar selvedges (Fig. 5B). These vein assemblages define a potassic alteration zone intersected towards the base of drill cores.

Weak propylitic alteration is evident at Bendigo (Table 1). Thin chlorite ± epidote veins (2–5 mm wide; P veins) cut the granodiorite (Fig. 5E). Locally, porphyritic diorite stocks experience intense to moderate alteration and display an overall reddish appearance, whereas plagioclase phenocrysts are selectively altered to an epidote-chlorite ± muscovite assemblage (Figs. 5G-H).

K-feldspar-biotite-magnetite-quartz veins (K3; Table 1) have been locally reopened by pervasive quartz-pyrite ± chalcopyrite ± molybdenite veinlets with greenish muscovite-quartz ± calcite selvedges (W1 vein; Figs. 5C-D). Planar quartz ± magnetite-pyrite ± bornite veins with thick greenish muscovite-quartz-pyrite envelopes (> 5 cm in width) commonly cut the medium-grained granodiorite (W2 vein; Figs. 5I and 7H). Chalcopyrite typically occurs as disseminations in quartz-pyrite veins, and locally as rims on pyrite crystals. Scanning electron microscopy-energy dispersive spectroscopy shows that chalcopyrite and bornite, and less common covellite and aikinite, occur as inclusions within pyrite grains (Figs. A3B–G).

Drill hole BD6 intersected a dark siltstone unit of the Umberatana Group from a depth of 79.2 m to its base. This siltstone contained abundant pyrite laminations and locally experienced hornfels alteration. Carbonate-quartz veins (CQ vein; Table 1) range from several mm to 1 cm in width and contain disseminated pyrite, molybdenite and trace amounts of chalcopyrite, which parallels or has a low angle to core direction (Fig. A3H). Locally, molybdenite-pyrite-bearing stockworks cut the siltstones (Fig. A3I).

Colebatch Mo prospect

This prospect is associated with a granitic intrusion exposed sporadically at the Colebatch South and North quarries, Richardson Rocks, and Tolmer Rocks in the southeast of South Australia (Fig. 1B; Table 1). The medium-grained intrusion is composed of K-feldspar (35-45 vol.%), quartz (30-35%), plagioclase (10-15%), and minor biotite (5-10%; Fig. 6A). Reconnaissance exploration recognized limited occurrences of molybdenite-quartz veins, approximately 5 mm to 1.5 cm in thickness (Fig. 6B), cutting the reddish granite. The molybdenite is medium- to coarse-grained (0.5–2 mm in diameter) and occurs as euhedral flakes. The Colebatch granite develops selectively weak chlorite-muscovite alteration.

Analytical techniques

LA-ICP-MS zircon U-Pb analysis

Zircons were hand-picked from heavy mineral concentrates of crushed granitic rocks under a petrographic microscope. Selected zircons were placed on double sided tape and were then set into 2.5-cm diameter epoxy blocks. These mounts were polished using clean sandpaper and polishing cloths. Cathodoluminescence (CL) and backscatter electron (BSE) images of zircons were collected simultaneously with a Hitachi SU3800 SEM operated at voltage of 15 kV, spot intensity of 80, and sample depth of ~10 mm, housed at Adelaide Microscopy in the University of Adelaide, in order to reveal internal textures and inclusions within individual zircons before U-Pb isotopic ratio analyses.

Zircon U-Pb analyses were performed at Adelaide Microscopy, using an Agilent 7900x quadrupole ICP-MS with a RESOlution 193nm ArF excimer laser system. Instrument mass bias and drift for $^{207}Pb/^{206}Pb$ ratios were corrected using NIST610 glass analyzed after every 20 unknowns (Baker et al., 2004). The GJ zircon (Jackson et al., 2004) was used to correct for Pb/U and Pb/Th mass bias, down hole fractionation, and instrument drift. Each zircon analysis began with a 30 s blank gas measurement followed by a further 30 s of analysis time when the laser was switched on. Zircons were analyzed with 30 µm spots and NIST610 glass with 43 µm spots, using a repetition rate of 5 Hz and an energy density of approximately 2 J/cm^2 (3.5 J/cm^2 for NIST610). A flow of He carrier gas (0.38 L/min) carried particles ablated by the laser out of the chamber to be mixed with Ar gas (1.01 L/min), which were then carried to the plasma torch. Secondary zircon reference materials were also analyzed: the 91500 (Wiedenbeck et al., 1995) and Plesovice (Sláma et al., 2008) zircons. Calculated weighted mean $^{206}Pb/^{238}U$ ages for GJ, 91500, and Plesovice zircons were 601.8 ± 1.0 Ma (n=36, 95% confidence, MSWD = 0.66), 1,059 ± 3.8 Ma (MSWD = 0.80), and 339.1 ± 0.9 Ma (MSWD=1.09), respectively, which are consistent within uncertainty of the recommended ages (e.g., Wiedenbeck et al., 1995; Jackson et al., 2004; Sláma et al., 2008). LA-ICP-MS data reduction was conducted using LADR software (https://norsci.com/ladr).

Zircon CL features, rare earth element contents, and U-Pb isotopic ratios were used to evaluate the data quality for each sample. U-Pb ages lying well above or below linear array of the dominant age population are likely either inherited grains, or grains that have undergone Pb loss. These analyses have been omitted from the final age calculation. Discordant grains were recognized if either their $^{206}Pb/^{238}U$ age divided by $^{207}Pb/^{235}U$ age was greater than 1 ± 0.05 or $^{206}Pb/^{238}U$ age divided by $^{207}Pb/^{206}Pb$ age was greater than 1 ± 0.15. Zircon grains ablated on CL-dark cores that give old dates were not included in the weighted mean age calculations, being predominantly discordant and/or anomalously old for the age of main magmatic population. Lanthanum concentrations > 2 ppm are considered to indicate the presence of apatite inclusions in zircon and these analyses

were also removed from consideration in the weighted mean age calculations. All weighted mean $^{206}Pb/^{238}U$ ages and analytical uncertainties for samples were calculated by Isoplot 4.15 and U-Pb Wetherill diagrams were plotted utilizing IsoplotR (Vermeesch, 2018). Both internal uncertainties from analysis and external uncertainties from analysis and decay constants are reported at 2σ level and presented in Table 3. The U-Pb isotopic results for standards and samples are tabulated in Appendix Table A1.

Re-Os molybdenite analysis

The analytical protocols of molybdenite separation and Re-Os isotope determinations by isotope dilution negative ion mass spectrometry (ID-NTIMS) were achieved following the protocols documented in Lawley and Selby (2012) and Li et al. (2017). Molybdenite-bearing quartz-pyrite veins were cut and crushed for molybdenite-rich quartz mixtures that were subsequently isolated from the host quartz veins using 48 wt.% HF treatment at room temperature and hand picking at the University of Adelaide, obtaining a separate purity ≥ 95%.

The Re-Os molybdenite analysis was conducted at the Durham Geochemistry Centre at Durham University (UK). Molybdenite separates were loaded into a Carius tube together with a tracer solution of ^{185}Re and normal Os and a 3:1 mix of 15.5N HNO_3 and 15.5N HCl, sealed, and digested at 220°C for ~24 hours. Osmium was isolated and purified from the acid medium using solvent extraction ($CHCl_3$) at room temperature and further purified using microdistillation. The Re fraction was isolated by NaOH-acetone solvent extraction and anion chromatography. The purified Re and Os fractions were loaded on to Ni and Pt wire filaments, respectively, and analyzed for their isotope compositions by negative thermal ionization mass spectrometry using static Faraday collectors on a Thermo TRITON mass spectrometer. Analytical uncertainties are propagated, and incorporate uncertainties related to Re and Os mass spectrometer measurements, blank abundances and isotopic compositions, spike calibrations, and reproducibility of standard Re and Os isotope values. During the course of this study Re and Os blanks were < 4 and 0.2 pg, respectively, with the $^{187}Os/^{188}Os$ blank of 0.23 ± 0.02. The Re-Os data with ^{187}Re decay constant, including its uncertainty (1.666×10^{-11}; Smoliar et al., 1996), were taken to calculate model Re-Os dates. The running average for the in-house Re and Os (DROsS) solution standards at the time analysis (September 2021) analyzed together with the sample analyses were 0.59861 ± 0.0015 and 0.16082 ± 0.0006, respectively. A synopsis of the molybdenite Re-Os data with 2σ level absolute uncertainties are presented in Table 2.

LA-ICP-MS/MS Rb-Sr analysis

White mica-bearing rocks were cut, mounted in epoxy, and polished (2.5 cm). The mineralogic and textural features (Fig. 7) were characterized by SEM-MLA (mineral liberation analysis) imaging using AMICS software, after collecting data from a Hitachi SU3800 SEM at Adelaide Microscopy. Laser ablation tandem inductively coupled mass spectrometer (ICP-MS/MS) Rb-Sr analyses were also conducted at Adelaide Microscopy, using an Agilent 8900 ICP-MS/MS instrument, coupled with a RESOlution ArF excimer 193nm laser ablation system, measuring both $^{87}Rb/^{86}Sr$ and $^{87}Sr/^{86}Sr$ ratios simultaneously. All samples were ablated in a He atmosphere (0.38 L/min) and mixed with Ar as the carrier gas (0.88 L/min) to the ICP, with 3.5 ml/min of N_2 added before the ICP torch to enhance the signal sensitivity. A reaction gas of N_2O was used to separate ^{87}Sr from ^{87}Rb within the reaction cell on the ICP-MS/MS. The carrier gas flow rates (He, Ar and N_2) and plasma conditions were tuned daily in normal "no-gas" mode (i.e., no gas in the reaction cell), using the NIST612 glass. Mica-Mg-NP of Hogmalm et al. (2017) was used as a primary reference material to correct for drift and instrument mass-bias. BCR-2G and NIST610 glass as well as GL-O glauconite with initial Sr ratio of 0.70735 (Boulesteix et al., 2020), Högsbo muscovite with initial Sr ratio of 0.70735 (Romer and Smeds, 1996), and MDC phlogopite with initial Sr ratio of 0.72607 (Hogmalm et al. 2017; Redaa et al., 2021) were analyzed as secondary reference materials. All reference materials were measured after every 20 unknown analyses. The expected ages for secondary micas standards are 95.1 Ma for GL-O, 1029 Ma for Högsbo, and 522 Ma for MDC, respectively (Romer and Smeds, 1996; Hogmalm et al. 2017; Boulesteix et al., 2020). Detailed protocols and parameters for LA-ICP-MS/MS analysis of mica Rb-Sr isotope ratios can be found in Redaa et al. (2021, 2022) and Subarkah et al. (2022). Data reduction for Rb-Sr isotope ratios was carried out using Iolite 3 software. Internal signal uncertainties were calculated within Iolite and propagated errors were calculated including the excess variance on MicaMg data using the weighted average function in Isoplot 4.15:

Propagated errors = sqrt ($A^2 + B^2$)

A = analysis internal signal error as %, B = excess variance on MicaMg as %.

The white mica Rb-Sr isochron ages are calculated by the maximum likelihood regression method using IsoplotR (Vermeesch, 2018), using ^{87}Rb decay constant of $1.3972 \pm 0.0045 \times 10^{-11}$ per year (Villa et al., 2015). All age uncertainties and error ellipses shown in isochron plots are at the 95% confidence level.

Six samples from Anabama Hill (AH20WH003, AH20WH007, AH20WH024, AH20WH026, AH20WH034A, and AH20WH086) were analyzed in the first session. Samples and reference materials were measured with a spot size of 67 µm, using a laser repetition rate of 10 Hz and an energy density of approximately 3.5 J/cm^2. Five samples from Netley Hill (NT21WH014, NT21WH026, NT21WH041, NT21WH047, and NT21WH067) were analyzed in the second session, along with three samples from Bendigo (BD20WH027B, BD21WH015C, and BD21WH031). These eight samples were measured with the same analytical conditions as the first session, except for a laser repetition rate of 5 Hz. Analyses at 10 Hz rather than 5 Hz produce younger ages for mica Rb-Sr dating, because of down-hole fractionation and matrix effects which affect the accuracy of $^{87}Rb/^{86}Sr$ ratios (Redaa et al., 2021). The $^{87}Sr/^{86}Sr$ ratios are consistent regardless of laser repetition rate. The first session analyses yielded Rb-Sr isochron ages for GL-O of 87.9 ± 2.4 Ma, Högsbo of 908 ± 17 Ma, and MDC of 498.7 ± 3 Ma. The mica Rb/Sr ratios and uncertainties in this session were corrected to the most reliable in-house standard MDC with a recommended age of 522 Ma (Redaa et al., 2021). The second session with a laser at 5 Hz produced Rb-Sr isochron ages for GL-O of 97.8 ± 4 Ma, Högsbo of 1014 ± 30 Ma, and MDC of 522 ± 8.2 Ma, which are consistent with their expected ages within analytical uncertainties (see above). A third analytical session was performed with same analytical parameters as the second session, which included three samples from the Bendigo prospects (BD20WH006, BD20WH045, and BD21WH013). Re-analyses of Anabama Hill white mica samples (AH20WH024-redo and AH20WH034A-redo) in the third session were used to confirm the accuracy of the secondary standard correction to MDC from the first session (see above). The Rb-Sr isotopic results for all samples and standards are tabulated in Appendix Table A2.

Analytical results

Cathodoluminescence imaging of zircon

Prismatic and/or stubby zircon crystals from the granites of the Delamerian porphyry prospects were texturally characterized by CL and BSE imaging, and their representative CL textures are presented in Figure 8. The zircon crystals range in length mostly from 50 to 450 µm and their length/width aspect ratios from 1:1 to 4:1 (Fig. 8). Sector and/or oscillatory growth zonings characterize these zircon crystals (> 2,000 grains) from the Delamerian porphyry prospects (Fig. 8). They show a typical well-developed pyramid shape, and many grains display core-to-rim oscillatory zoning patterns with alternating CL-bright and CL-grey intensity (Fig. 8). A number of zircon grains have sub-rounded, homogeneous cores with bright CL response rimmed by fine-

scale oscillatory dark to grey CL growth (Figs. 8B and 8D-F), or CL-dark homogeneous core with CL-bright oscillatory rims (Figs. 8G-K). Some grains have symmetric CL-bright sector zones in the core domain, defining an hourglass morphology (e.g., Fig. 8F). Most of the zircon grains from the Colebatch prospect are characterized by subtle bright to dark CL sector zoning with rare oscillatory zoned rims (Fig. 8L). The average Th/U ratios in zircon from these Delamerian granitoids range mostly from 0.57 to 2.2 (Appendix A1). The well-developed growth zoning patterns and Th/U ratios undoubtedly illustrate that these zircons are of magmatic origin (Th/U commonly ≥ 0.5; cf. Hoskin and Schaltegger, 2003). The CL-dark cores are interpreted to be inherited zircons and thus were avoided during U-Pb isotopic analysis. Some large zircon crystals (> 200 µm in length) contained one or more silicate inclusions that were also avoided during LA-ICP-MS analyses.

Zircon LA-ICP-MS U-Pb dates

Anabama Hill. Nine of thirty individual LA-ICP-MS zircon analyses yielded a weighted average $^{206}Pb/^{238}U$ age of 484.2 ± 4.0 Ma (including uncertainty of all sources of analytical uncertainty and decay constant; MSWD = 1.7; n =9/30; Fig. 9A) for the granodiorite (AH20WH065) at Anabama Hill. One analysis gives a young $^{206}Pb/^{238}U$ age of 376.4 Ma, possibly resulting from Pb loss. Three analyses returned old $^{206}Pb/^{238}U$ ages from 507 to 536 Ma. These results together with another analyses (discordant grains) are not included in U-Pb age calculation. The measured date (484.2 ± 4.0 Ma) is in accordance with the zircon Pb-Pb plateau age of 485 ± 4 Ma reported by Nasev (1998).

The plagioclase-phyric diorite (AH20WH007) cutting the granodiorite defined a weighted mean $^{206}Pb/^{238}U$ date of 472.0 ± 3.9 Ma (MSWD = 1.5; n=10/30; Fig. 9B). One zircon measurement gave a Mesoproterozoic $^{206}Pb/^{238}U$ date of 1281 Ma that was ablated on an inherited CL-dark zircon core. Another 19 analyses identified as discordant zircon grains (e.g., rho <0 or La > 2 ppm) were discarded for age determination.

The monzogranite (AH20WH032) intruding the granodiorite batholith and diorite at the bottom of drill hole DDHAN7 (628–796m) gave a weighted $^{206}Pb/^{238}U$ date of 470.4 ± 3.1 Ma (MSWD = 1.02; n = 7/30; Fig. 9C). Five spot analyses have young $^{206}Pb/^{238}U$ ages ranging from 433 to 159 Ma and two grains have old ages of 583–533 Ma. Another 21 discordant grains (rho < 0 or anomalously high REEs) were discarded from U-Pb age determination.

The porphyritic dike (AH20WH003) overprinted by intensive muscovite-quartz-pyrite alteration (Fig. 3E) defined a weighted $^{206}Pb/^{238}U$ age of 469.1 ± 3.7 Ma (MSWD = 1.2; n = 8/30; Fig. 9D). Three analyses revealed

old $^{206}Pb/^{238}U$ ages of 572–509 Ma, suggesting some inheritance, and eleven younger $^{206}Pb/^{238}U$ ages from 160 to 434 Ma suggest some degree of Pb loss. Five analyses with $^{206}Pb/^{238}U$ ages of 451 to 481 Ma are interpreted to be discordant. Two analyses have anomalous Nb > 20 ppm. These discordant results are excluded from the U-Pb age calculation.

Netley Hill. The grey granodiorite with equigranular texture (NT21WH027) at Netley Hill gave a weighted mean $^{206}Pb/^{238}U$ date of 476.4 ± 2.5 Ma (MSWD = 0.95; n = 14/30; Fig. 10A). One result showed a young $^{206}Pb/^{238}U$ date of 369 Ma, as a consequence of Pb loss. Four analyses revealed old $^{206}Pb/^{238}U$ dates from 512 to 546 Ma. Another ten results were identified as discordant grains (i.e. rho < 0) were also removed for U-Pb age determination.

The reddish K-feldspar granite (NT21WH045) defined a weighted $^{206}Pb/^{238}U$ mean date of 478.2 ± 4.5 Ma (MSWD = 1.6; n = 9/30; Fig. 10B). Three spot analyses presented Neoproterozoic $^{206}Pb/^{238}U$ ages ranging from 775 Ma to 670 Ma, reflecting ablation on inherited old cores. Eight analyses revealed a cluster of young $^{206}Pb/^{238}U$ ages of 438–27 Ma, possibly illustrating various magnitudes of Pb loss. Another seven analyses were discordant grains due to age outliers and/or negative rho and not included in the weighted mean age calculation.

The dioritic dike at Netley Hill (NT21WH055) yielded a weighted mean $^{206}Pb/^{238}U$ date of 470.8 ± 2.1 Ma (MSWD = 0.87; n = 13/30; Fig. 10C). Five analytical results were not included for age calculation, because they had Neoproterozoic to early Cambrian ages of 855 Ma to 507 Ma ascribed to inheritance. Another 12 analyses were considered as discordant ages, being owning to Pb loss, negative rho, or anomalously high trace element contents, which were not included for U-Pb age determination, either.

The biotite-phyric granite (NT21WH028) at Netley Hill defined a weighted $^{206}Pb/^{238}U$ mean date of 477.9 ± 2.7 Ma (MSWD = 1.09; n = 9/30; Fig. 10D). Three young LA-ICP-MS spot analyses revealed dates from 400 Ma to 301 Ma, an old date of 496 Ma, and 18 discordant grains (rho < 0 or high REE contents). These results were not included in the weighted mean age determination.

Bendigo. The coarse-grained granodiorite (BD20WH047) from the Bendigo prospect yielded a weighted average $^{206}Pb/^{238}U$ date of 490.6 ± 1.7 Ma (MSWD = 0.91; n = 22/30; Fig. 11A). Eight zircon spot analytical results were removed, as they either were heavily contaminated by micro-scale inclusion or were considered discordantly (old or young age outliers).

The biotite granite (BD20WH040) at Bendigo gave a weighted mean $^{206}Pb/^{238}U$ date of 488.8 ± 2.0 Ma (MSWD = 1.14; n = 13/30; Fig. 11B). Nine zircons yielded discordant U-Pb age groups of 632 to 537 Ma and 405 to 399 Ma, respectively, which can be explained by mixed Neoproterozoic core or Pb loss. These results were culled from U-Pb age calculation.

The porphyritic dike (BD21WH014) produced a weighted mean $^{206}Pb/^{238}U$ date of 484.5 ± 2.6 Ma (MSWD = 0.67; n = 8/30; Fig. 11C). Eight analytical results were culled due to inheritance with age from 603 to 528 Ma. Another 14 analyses were considered discordant grains and removed from the age calculation.

Colebatch. The equigranular Colebatch granite sample (CB20WH01) defined a weighted $^{206}Pb/^{238}U$ mean age of 478.2 ± 2.7 Ma (MSWD = 0.97; n = 13/30; Fig. 11D). Three analyses were heavily contaminated by micro-scale inclusions based on time-resolved element spectra. Seven results gave old $^{206}Pb/^{238}U$ ages of 524–661 Ma, reflecting inheritance of CL-dark old zircon cores. Another seven zircon analyses were identified as discordant grains due to Pb loss or negative rho. These zircon U-Pb ratio results were removed for age calculation.

Molybdenite Re-Os dates

Anabama Hill. Molybdenite in sample AH20WH014 from the Anabama Hill prospect occurs as fine-grained (<1 mm in diameter) aggregates associated with moderate- to coarse-grained muscovite, within massive quartz-pyrite matrix (> 10 cm in length) at a depth of 197 m in drill hole DDHAN7. A second sample, AH20WH062, of fine-grained disseminated molybdenite associated with an intensively veined quartz-pyrite-muscovite assemblage was taken from 110 m in drill hole ANDDH2 (Fig. 2A). The two Anabama Hill molybdenite separates had comparable Re and ^{187}Os concentrations: 44.7–31.3 ppm and 217–152 ppb, respectively. They yielded near-identical Re-Os dates (including uncertainty of all sources of analytical uncertainty and decay constant) of 462.9 ± 2.4 Ma and 462.7 ± 2.4 Ma, respectively (Table 2).

Netley Hill. One molybdenite sample (NT21WH039) from the Netley Hill prospect was collected from a molybdenite-pyrite-quartz vein cutting a red fine-grained aplite at a depth of 192 m in drill hole NTDD001. This molybdenite sample contained 190 ppm Re and 935 ppb ^{187}Os and yielded a Re-Os date of 465.6 ± 2.4 Ma (Table 2), similar to Re-Os ages at Anabama Hill (463 ± 2.4 Ma).

Bendigo. Sample BD21WH027 was taken from a 5 cm-wide molybdenite-pyrite-quartz vein cutting the Bendigo granite, where it had experienced intense argillic alteration at a depth of 112 m in drill hole BD5. A second

sample (BD21WH033) was taken from a molybdenite-pyrite-quartz-carbonate vein with a width of 0.5–1 cm, truncating a dark siltstone sequence in drill hole BD6 at a depth of 83 m. The BD21WH033 molybdenite had 385.3 ppm Re and 1,901 ppb ^{187}Os, much higher than those in sample BD21WH027 (55.3 ppm and 278 ppb, respectively; Table 2). The Re-Os data yielded distinct model dates of 477.7 ± 2.5 Ma (BD21WH027) and 469.4 ± 2.4 Ma (BD21WH033; Table 2).

Colebatch. Sample CB20WH01 is a hand specimen from the Colebatch prospect, in which a coarse-grained molybdenite vein (0.5–1 cm wide) cuts the equigranular granite (Fig. 6B). The analyzed molybdenite contained 10.8 ppm Re and 50 ppb ^{187}Os, and defined a Re-Os date of 477.9 ± 2.5 Ma (Table 2).

In situ white mica Rb-Sr dates

Anabama Hill. Six white mica-quartz-pyrite-bearing polishing rock mounts from the Anabama Hill prospect were analyzed by LA-ICP-MS/MS for *in situ* Rb-Sr isotopic determination (Table 3), and two samples were repeated for analysis (AH20WH024-redo and AH20WH34A-redo). Two white mica-quartz-pyrite veins cutting the epidote-altered granodiorite were analyzed (AH20WH024 and AH20WH086). The AH20WH024 white mica-quartz vein defined a Rb-Sr isochron date of 443.9 ± 7.5 Ma (including analytical and decay constant uncertainties, MSWD = 1.8; n = 46), with an initial ^{87}Sr/^{86}Sr ratio of 0.6991 ± 0.0145 (^{87}Sr/^{86}Sr$_i$; Fig. 12A). The repeated analyses defined a Rb-Sr isochron age of 451.5 ± 4.6 Ma (MSWD = 0.54; n = 52) and a regressed ^{87}Sr/^{86}Sr$_i$ ratio of 0.7071 ± 0.0072 (Fig. 12B). Sample AH20WH086, a white mica-quartz vein overprinting chlorite-epidote alteration (Fig. 7A), gave a Rb-Sr isochron date of 449.8 ± 13.8 Ma (MSWD = 1.3; n = 41), with an ^{87}Sr/^{86}Sr$_i$ value of 0.7016 ± 0.0102 (Fig. 12C).

Disseminated white micas from two altered diorite rocks (AH20WH007 and AH20WH026) were analyzed from Anabama Hill. These white micas are fine-grained, typically 10–100 μm in size and are hydrothermal replacement products after plagioclase phenocrysts. A Rb-Sr isochron date of 439.1 ± 12.4 Ma (MSWD =1.4; n = 43/44) was acquired for the AH20WH007 sample, with an ^{87}Sr/^{86}Sr$_i$ value of 0.7030 ± 0.0061 (Fig. 12D). Fine-grained white micas cut by an epidote-pyrite ± chalcopyrite vein (Fig. 7B) from the AH20WH026 sample gave a Rb-Sr isochron date of 445.1 ± 14.8 Ma (MSWD = 0.86; n = 42/46) and an ^{87}Sr/^{86}Sr$_i$ ratio of 0.7010 ± 0.0059 (Fig. 12E).

One euhedral, coarse-grained muscovite-quartz vein (1-2 cm wide) with minor disseminated pyrite cutting the monzogranite (AH20WH034A; Fig. 7C) produced a Rb-Sr isochron age of 454.4 ± 8.5 Ma (MSWD = 1.0;

n = 45) and an $^{87}Sr/^{86}Sr_i$ value of 0.6945 ± 0.0115 (Fig. 12F). This sample was re-analyzed during the third session, giving a Rb-Sr isochron date of 447.3 ± 7.4 Ma (MSWD = 0.6; n = 56), with a regressed $^{87}Sr/^{86}Sr_i$ value of 0.7009 ± 0.0088 (Fig. 12G).

White mica-pyrite-quartz overprinting the porphyritic dike (AH20WH003) yielded a Rb-Sr isochron date of 439.6 ± 13.2 Ma (MSWD = 0.98; n = 37/48), with an $^{87}Sr/^{86}Sr_i$ ratio of 0.7080 ± 0.0099 (Fig. 12H). Eleven analyses were not included in the Rb-Sr isochron calculation due to accidental ablation of non-mica minerals or contamination by other solid inclusions.

Netley Hill. Five white mica-quartz-pyrite-bearing veins, veinlets, and/or breccias at Netley Hill were analyzed (Table 3). White micas from a biotite-phyric dike (NT21WH026) overprinted by moderate to intense white mica-quartz-magnetite-pyrite alteration yielded a Rb-Sr isochron date of 449.7 ± 5.3 Ma (MSWD = 0.88; n = 44), with an $^{87}Sr/^{86}Sr_i$ ratio of 0.7027 ± 0.0060 (Fig. 13A).

Sample NT21WH014 comes from an aplite-clast breccia that is predominantly cemented by quartz and white mica (Fig. 7D) from drill hole NTDD002 at a depth of 134.5 m from the Netley Hill prospect. White micas from sample NT21WH014 yielded a Rb-Sr isochron date of 461.3 ± 18.7 Ma (MSWD = 0.59; n = 42/48), after culling six analyses with high $^{87}Rb/^{86}Sr$ (>430) and $^{87}Sr/^{86}Sr$ ratios (>17). These results produced a regressed $^{87}Sr/^{86}Sr_i$ ratio of 0.657 ± 0.052 (Fig. 13B).

Massive white mica and quartz alteration from drill hole NTD001 at depth of 210 m (Fig. 7E; NT21WH041) and associated with K-feldspar-chalcopyrite veins that cut a plagioclase-phyric diorite defined a Rb-Sr isochron date of 459.6 ± 15.9 Ma (MSWD = 0.86; n = 45) and returned an $^{87}Sr/^{86}Sr_i$ ratio of 0.684 ± 0.027 (Fig. 13C).

White mica crystals from a grey equigranular granite that has intense muscovite-quartz-pyrite alteration (NT21WH047; Fig. 7F) gave a Rb-Sr isochron date of 446.3 ± 12.5 Ma (MSWD = 1.0; n = 44) and an $^{87}Sr/^{86}Sr_i$ ratio of 0.691 ± 0.025 (Fig. 13D). White micas from the equigranular granite (NT21WH067) cut by K-feldspar-pyrite-chalcopyrite veins were analyzed. This sample was overprinted by massive white mica-quartz-pyrite ± magnetite alteration, forming granitic clast-supported, jigsaw breccias. The analyses gave a Rb-Sr isochron date of 435.9 ± 16.3 Ma (MSWD = 0.88; n = 45) and an $^{87}Sr/^{86}Sr_i$ value of 0.715 ± 0.038; Fig. 13E).

Bendigo. Six white mica-quartz-pyrite-bearing veins and veinlets from the Bendigo prospect were selected for Rb-Sr isotopic measurements (Table 3). White mica alteration in the plagioclase-phyric diorite (BD20WH006;

Fig. 7G) yielded a Rb-Sr isochron date of 458.6 ± 8.8 (MSWD = 2.8; n = 38) and an $^{87}Sr/^{86}Sr_i$ ratio of 0.7019 ± 0.0091 (Fig. 14A).

Two white mica-bearing samples were measured from the granodiorite at the Bendigo prospect. Sample BD21WH031 is from drill hole BD5, in which the granodiorite is strongly altered by massive greenish mica, quartz, and pyrite (Fig. 7I). The BD21WH015C sample is characterized by a thick white mica-quartz-pyrite-chalcopyrite-molybdenite vein (2–3 cm wide) cutting albite-altered granodiorite from BD7 (Fig. 7H). A Rb-Sr isochron date of 470.2 ± 16.9 Ma (MSWD = 0.76; n = 45/46) and an $^{87}Sr/^{86}Sr_i$ ratio of 0.71 ± 0.11 was obtained for the BD21WH015C white micas (Fig. 14B); one result with $^{87}Rb/^{86}Sr$ value of 5,000 was not included for isochron regression. The BD21WH031 white micas defined a Rb-Sr isochron date of 478.3 ± 18.1 Ma (MSWD = 0.66; n = 32). These analyses regressed an imprecise $^{87}Sr/^{86}Sr_i$ value of 0.57 ± 0.21 (Fig. 14C), although its upper-end value partially overlaps other regressed $^{87}Sr/^{86}Sr_i$ compositions (e.g., 0.70–0.72).

Three white mica samples were analyzed from the biotite granite at the Bendigo prospect. Sample BD21WH013 is characterized by a thin muscovite-pyrite vein (1–2 mm wide) cutting moderate K-feldspar-epidote alteration and gave a Rb-Sr isochron date of 471.9 ± 3.9 Ma (MSWD = 0.91; n = 50), with an $^{87}Sr/^{86}Sr_i$ ratio of 0.7001 ± 0.0112 (Fig. 14D). The granite overprinted by quartz-pyrite-white mica veins (BD20WH045) produced a Rb-Sr isochron date of 465.6 ± 4.4 Ma (MSWD = 1.2; n = 48/53), with an $^{87}Sr/^{86}Sr_i$ ratio of 0.7034 ± 0.0066 (Fig. 14E), after culling five non-mica analyses with anomalous high $^{87}Rb/^{86}Sr$ ratios (>3,000). The white micas from a reddish biotite granite that has intense white mica-pyrite-quartz alteration (BD20WH027B) defined a Rb-Sr isochron date of 459.5 ± 6.7 Ma (MSWD = 1.4; n = 44) and an $^{87}Sr/^{86}Sr_i$ ratio of 0.6979 ± 0.0189 (Fig. 14F).

Discussion

Multiple pulses of magmatism

The eight new LA-ICP-MS zircon U-Pb ages from Anabama illustrate that multiple magmatic emplacement events occurred in the region, ranging approximately from 485 to 465 Ma (Figs. 9–10 and 15). The granodiorite sill that dominates the Anabama Granite was the oldest intrusive phase at Anabama Hill and Netley Hill prospects, being emplaced between 488 and 475 Ma (Table 3; Fig. 15). The diorite and monzogranite were emplaced during intermittent magmatism over the period ca. 475–470 Ma at the two prospects (Table 3; Fig.

15). The presence of granodioritic enclaves contained in the diorite and monzogranite phases at Anabama Hill prospect (Fig. 3C) is also consistent with the geochronological evidence. The porphyritic dacite dike (469.1 ± 3.7 Ma) is within analytical uncertainty of the second magmatic phase (475–470 Ma; Fig. 15), but may be the youngest intrusion in the Anabama Granite.

Petrographic observation indicates that diorite dikes and biotite-bearing granite intruded after the coarse-grained granodiorite at Bendigo, based on observed contact relationships and the occurrence of granodiorite enclaves within the diorite dikes. This is consistent with our zircon U-Pb dating results (Figs. 11A-C and 15) which yielded 490.6 ± 1.7 Ma for the granodiorite and 488.8 ± 2.0 Ma for biotite granite, which predate the plagioclase-phyric diorite by ca. 5 m.y., with the latter being emplaced at 484.5 ± 2.6 Ma.

Zircon LA-ICP-MS analyses yield a U-Pb age of 478.2 ± 2.7 Ma for the granite at Colebatch in the southern portion of the Delamerian Orogen (Fig. 15). Its age largely overlaps with other A-type granites (e.g., Mannum, Padthaway, Marcollat, Monteith, and Kongal etc.) in the adjacent Padthaway Ridge region of South Australia, which range from 485 to 475 Ma (Fig. 16B; Turner et al., 1992; Foden et al., 2020).

Intrusion of Bendigo Granite including the granodiorite, diorite and biotite granite variants, and the Anabama granodiorite, occurred at the end of the 514–490 Ma Delamerian Orogeny (Foden et al., 2006). They were emplaced in the response to the Pacific oceanic lithosphere being subducted beneath the passive South Australian craton margin, marking the final stages of Gondwana Supercontinent assembly (Fig. 16A; Foden et al., 2002, 2020). The diorite, monzogranite, and porphyry dacite dikes at Anabama and the Colebatch granite were emplaced from 475 Ma to 465 Ma, and postdate the Delamerain Orogen. They were associated with a period of post-tectonic magmatism, slab roll-back and tearing, isostatic uplift, and exhumation in the Delamerian Orogenic Belt (Fig. 16B; Foden et al., 2006, 2020), during which eastward step-back of the Pacific oceanic slab led to re-initiation of subduction beneath the Macquarie Arc in New South Wales (Fig. 16B; Lickfold et al., 2003; Crawford et al., 2007; Glen et al., 2007a; Kemp et al., 2009).

Timing of porphyry mineralization

Molybdenite Re-Os chronology is one of the most robust chronometers – it has been used widely to date sulfide mineralization associated with magmatic intrusions, especially to recognize different hydrothermal mineralized episodes (Wilson et al., 2007; Lawley and Selby, 2012; Chiaradia et al., 2013; Li et al., 2017; Pollard et al., 2021). Six molybdenite samples separated from K-feldspar-quartz-chalcopyrite and muscovite-

quartz-pyrite veins likely reveal two porphyry-style mineralization events in the Delamerian Orogen of South Australia (Fig. 15; Table 3). The earlier Cu-Mo sulfide mineralization event appears to have occurred between 480 and 475 Ma, as detected in the Bendigo (477.8 ± 2.5 Ma) and Colebatch (477.9 ± 2.5 Ma) prospects (Fig. 15). The Re-Os molybdenite ages imply the potential presence of granitic stocks and/or porphyritic phases of ca. 482 Ma (e.g., the plagioclase-phyric dike) being causative to this porphyry-style mineralization event. The Re-Os age of 477.9 ± 2.5 Ma from a molybdenite-quartz vein at Colebatch overlaps the zircon U-Pb age of its host granite (478.2 ± 2.7 Ma; Fig. 11D and 15).

A second porphyry-style Cu-Mo mineralization event has been revealed by four molybdenite Re-Os ages ranging from 470 to 460 Ma from the Anabama Hill, Netley Hill, and Bendigo prospects (Table 3; Fig. 15). Two identical Re-Os ages of 462.8 ± 2.4 Ma from pyrite-muscovite-quartz veins, although nominally younger, within uncertainty, are consistent with the porphyritic dikes with zircon U-Pb date of 469.1 ± 3.7 Ma at Anabama Hill (Fig. 15), whereas a Re-Os age of 465.5 ± 2.4 Ma from a molybdenite-pyrite-quartz vein cutting porphyritic aplite at Netley Hill largely overlaps with U-Pb dates of 475–465 Ma for the granitoids (Fig. 15). These data imply that the porphyritic dikes and stocks are likely the causative magma sources to porphyry Cu-Mo mineralization associated with the Anabama Granite. A Re-Os age of 469.4 ± 2.4 Ma has been determined for a pyrite-quartz-carbonate vein cutting a Neoproterozoic siltstone sequence at Bendigo. It is ca. 5–10 m.y. younger than that for the molybdenite-pyrite-quartz vein cutting argillically altered granite (Fig. 15), and probably represent later hydrothermal sulfide mineralization or remobilization led by a causative intrusion at depth that is not yet identified or sampled in the currently available drill holes.

The recorded porphyry Cu-Mo mineralization of 470–460 Ma in the Delamerian Orogen slightly overlaps with the early porphyry mineralization event of 467–455 Ma (e.g., Marsden, E43, and Milly Milly) in the Cowal Lake district of Lachlan Orogenic Belt, bracketed by zircon U-Pb and/or molybdenite Re-Os geochronology (Zukowski, 2010; Rush, 2013; Forster et al., 2015; Leslie et al., 2021; Figs. 15-16). However, the widespread porphyry Cu-Au mineralization occurred from 445 to 437 Ma in the Cadia, Northparkes, and Lake Cowal districts of the Ordovician Macquarie Arc (Lickfold et al., 2003; Wilson et al., 2007; Harris et al., 2020; Leslie et al., 2021; Fig. 15) that superimpose on the eastern margin of the Delamerian Orogen.

Protracted history of magmatic-hydrothermal alteration?

The repeated Rb-Sr isotopic analyses using 5 Hz laser frequency for white micas from granodiorite and monzogranite samples at Anabama Hill yield isochron ages that are within analytical uncertainties (ca. 7–8 Ma, 2σ precision < 1.8 %) comparable to the ages obtained with laser operated at 10 Hz (Fig. 12A vs. 12B and Fig. 12F vs. 12G). This demonstrates the feasibility of Rb/Sr ratio calibration using the most reliable in-house standard MDC aged at 522 Ma. Overall, 19 *in situ* white mica Rb-Sr isochron ages from the Delamerian porphyry system have a broad range from 478 to 435 Ma (Table 3), and roughly define two temporal episodes of 480–460 Ma and 450–435 Ma, respectively (Fig. 15). Among these Rb-Sr isochron ages, nine results have analytical uncertainties less than 9 Ma, within 2 % precision, whereas another ten age results have large analytical uncertainties of > 12 Ma, with precision up to 4 % (2σ; Fig. 15; Table 3). However, all the Rb-Sr isotopic results display well-defined isochrons (Figs. 12–14). The regressed initial Sr isotopic values mostly change from 0.7001 to 0.715, except one result of 0.57 ± 0.21 (i.e., BD21WH031; Fig. 14C), largely consistent with whole-rock $^{87}Sr/^{86}Sr_{initial}$ compositions for granodiorite (0.7070–0.7085) and dacite porphyries (0.7047–0.7181) at Anabama Hill and Netley Hill (McDonald, 1992). Therefore, white mica Rb-Sr isochron ages reported in this study are considered to have geologic importance and most of the age scatter is likely to be analytical rather than geologic, given that some of the magnitude of age uncertainties are as large as 3 to 4 % precision.

A Rb-Sr isotopic age of 478 ± 18 Ma was determined for intense white mica-quartz alteration in the granodiorite stock at Bendigo, corresponding to the early porphyry-style mineralization stage defined by the Re-Os molybdenite age of 478 ± 2.5 Ma (Fig. 15). Three Rb-Sr isochron ages range from 472 to 465 Ma for white mica-quartz-pyrite ± chalcopyrite veins at Bendigo prospect (Fig. 14) and are comparable to the late porphyry-style mineralization event around 470 Ma identified through Re-Os molybdenite chronology (Fig. 15). Two white mica-bearing samples from the Bendigo diorite porphyry and biotite granite yield Rb-Sr isochron ages around 460 ± 8 Ma, 5–10 m.y. younger than the timing for the second porphyry-style mineralization event (Fig. 15).

Only two white mica Rb-Sr ages of 460 ± 15 Ma from the Netley Hill prospect are consistent with those gained from zircon U-Pb and molybdenite Re-Os methods and associated with the timing of porphyry-style mineralization (465–460 Ma) at Anabama Hill and Netley Hill (Fig. 15; Table 3). Eleven white mica Rb-Sr isotopic dates from the Anabama Hill and Netley Hill prospects fall into a younger range of 455 to 435 Ma (Fig. 15), which might represent a prolonged hydrothermal alteration and cooling history, over a period of 10 to 25

m.y. after the main porphyry-style Cu-Mo mineralization event at Anabama Hill. However, it is noted that the typical duration of a porphyry-style hydrothermal mineralization event is suggested to last from 0.1 to 2 m.y. (Chiaradia et al., 2013; Li et al., 2017). It is therefore unlikely that this prolonged cooling history recorded by the Rb-Sr isotopic dates are directly associated with the porphyry-style mineralizing event.

Alternatively, the wide age range of 455 to 435 Ma for white micas at Anabama Hill and Netley Hill may have been accounted for a distinct regional thermal disturbance event, owing to the low closure temperature of Rb-Sr isotopic system in mica (ca. 300°C; Blanckenburg et al., 1989; Chiaradia et al., 2013). Muscovite- and chlorite-rich phyllites from the Mount Lofty Ranges and Fleurieu Peninsular of the Delamerian Orogen yielded $^{40}Ar/^{39}Ar$ spectrum ages of 458 to 430 Ma (Fig. 15; Reid et al., 2022). These ages have been interpreted as a result of far-field geodynamic events along the eastern paleo-Pacific margin of Gondwana (Reid et al., 2022; Fig. 15). All the white mica Rb-Sr and $^{40}Ar/^{39}Ar$ ages appear to have correlated with thermal events occurring in the adjacent Lachlan Orogen, which experienced an episode of arc reversal at 455–450 Ma (Meffre et al., 2007) and two peaks of compressive deformation during the Benambran Orogeny (~443 and ~430 Ma; Glen et al., 2007b; Harris et al., 2020). The same thermal event may also have affected the Rb-Sr isotopic system recorded in white micas at Anabama Hill and Netley Hill.

Implications for metallogenic setting

Ultramafic-mafic and intermediate-felsic rocks in the Adelaide Fold Belt and adjacent regions in western Victoria and New South Wales provide important evidence for the geodynamic evolution of the Delamerian Orogen. Cambrian basalt lavas in this orogenic belt saw a change from alkaline to tholeiitic composition during the period 520–515 Ma (Foden et al., 2020). The mafic magmatism is interpreted to have derived from an evolving mantle wedge modified by asthenospheric upwelling and continental contamination, defining a rifting-related back arc setting under extension (Foden et al., 2020). A newly recognized quartz diorite at 516 ± 1.5 Ma from beneath the South Australian Murray Basin shows geochemical affinities similar to those formed in a subduction environment, and an undated boninitic rock near the township of Keith displays a depleted mantle character, both suggesting the initiation of subduction of Pacific oceanic lithospheric slab as early as ca. 520 Ma (Fig. 16A; Foden et al., 2020). Boninitic suites, calc-alkalic basalts, and/or volcanic-arc granites were also reported in the Mt Stavely Arc of Victoria and Koonenberry Belt of New South Wales and fall into an interval of 510–500 Ma, marking the triggering of subduction in these two districts (Fig. 16A; Kemp, 2003; Greenfield

et al., 2011; Johnson et al., 2016; Schofield, 2018). This leaves an approximately 10 m.y. period to have forged eastward slab rollback and retreat in the southeast of South Australia, accompanied with the progressive migration of the west-dipping subduction zone to neighboring states in the Cambrian.

Although the driver for Delamerian deformation remains unclear, there is strong evidence suggesting that the convergent deformation and metamorphism in this orogen occurred between ca. 514 and ca. 490 Ma (Fig. 16A; Flöttmann et al., 1998; Foden et al., 2006, 2020). The granitic Rathjen Gneiss is the oldest felsic intrusion in the Delamerian Orogen with a crystallization age of 514 ± 5 Ma and shows a distinctive tectonic foliation and geochemical affinity comparable to within-plate or anorogenic granites (Foden et al., 1999). Zircon overgrowths on igneous grains constrain the timing of metamorphism to 503 ± 7 Ma during the Delamerian Orogeny (Foden et al., 1999). Syn-tectonic I- and S-type granites outcrop mainly in the eastern portion of the Mt Lofty Ranges, the Fleurieu Peninsula (e.g., Victor Harbor), and Kangaroo Island, ranging in age from 505 to 490 Ma (Fig. 16A), and show geochemical characteristics and textures similar to typical granites in syn-collisional environments (Foden et al., 2002, 2006). The cessation of the Delamerian Orogeny was followed by emplacement of Ordovician bimodal, undeformed granites over a period of ~ 20 m.y. until 470 Ma (Fig. 16B; Foden et al., 2006, 2020).

Our zircon U-Pb ages have extended the age range of this post-tectonic felsic magmatism phase in the Nackara Arc of the Delamerian Orogen to ca. 460 Ma (Figs. 15-16B; Table 3). Importantly, our new zircon U-Pb, molybdenite Re-Os, and white mica Rb-Sr geochronologic ages indicate that porphyry Cu-Mo mineralization occurred at ca. 480–460 Ma, subsequent to subduction and basin formation, metamorphism, and deformation across the Delamerian Orogen (Fig. 16B). These dates are also similar to ca. 470–458 Ma ages for deformation obtained from thrust sheets in the western region of the orogen (Reid et al., 2022), suggesting that tectonic activity certainly did not cease with the emplacement of ca. 490–470 Ma granitoids. Foden et al. (2006, 2020) proposed that these 490–470 Ma granitoids formed due to delamination of a dense mafic underplate (e.g., eclogite) near Moho depths and associated asthenospheric upwelling (Fig. 16B). Our data now show this mantle upwelling also resulted in magmatism to as young as ca. 460 Ma. Delamination of depleted mantle lithosphere and/or simultaneous slab rollback can lead to partial remelting of the prior subduction-modified arc lithosphere and hydrous lower crustal cumulates enriched in chalcophile and siderophile elements, producing aqueous oxidized magmas that are potentially conducive for porphyry-style mineralization (Fig. 16B; Richards, 2009; Richards and Mumin, 2013). Using this model, translithospheric structures provide pathways for the rapid ascent

of magmas and are important exploration criteria (cf. Cooke et al., 2014). Applied to the Nackara Arc region of the Delamerian Orogen, mineralized magmas and fluids are likely to have ascended along favorable structures/corridors to shallow crust levels (3–10 km), within the locus where Cu-bearing sulfides precipitated with multi-stage magmatic-hydrothermal veining and breccias in porphyry-style systems at Anabama Hill, Netley Hill, and Bendigo prospects (Fig. 16B). Since these porphyry-style magmatic-hydrothermal systems occur subsequently to the subduction that initially formed the Cambrian back-arc basin into which the Kanmantoo and Normanville groups were deposited, we suggest that they can be viewed in this sense as post-subduction. The upwelling and partial melting of metasomatized Delamerian subcontinental lithospheric mantle are a likely source for the mineralizing fluids (Fig. 16B). The setting in which the Delamerian porphyry systems formed is considered favorable loci for generation of porphyry copper ± molybdenum ± gold deposits (cf. Wilson et al., 2007; Richards, 2009; Cooke et al., 2014).

Our new geochronological data provide encouraging implications to aid mineral exploration in the Delamerian Orogen. Possible targets are porphyritic stocks, dikes, and apophyses with magmatic ages of 470–460 Ma. Because porphyritic dikes and apophyses are vulnerable to intense magmatic-hydrothermal alteration, detailed logging is necessary to identify and map their distributions and to track ore-forming fluid footprints. Further geochronology and mineral chemistry would also assist defining the location and fertility of these intrusive rocks herein. Future exploration and research activities in this belt are recommended to report comprehensive lithogeochemical results (including gold) so as to further elucidate petrogenesis of the host rocks and evaluate fertility of the systems.

Conclusions

A reconnaissance study of the Anabama Hill, Netley Hill, Bendigo, and Colebatch porphyry prospects in the Delamerian Orogen of eastern South Australia has shown that their hydrothermal alteration and mineralization characteristics are comparable to typical porphyry Cu-Mo deposits, with Cu-bearing sulfides being hosted by veins, stockworks, and minor breccias that genetically and spatially related to Early-Middle Ordovician granitic intrusions. Weak to moderate K-feldspar and chlorite-epidote alteration are associated within these prospects that have been overprinted by intense muscovite-quartz-pyrite alteration. Zircon U-Pb ages reveal multiple pulses of granitoid emplacement, ranging from 490 to 460 Ma in the Delamerian Orogen. Precise molybdenite Re-Os geochronology indicates two porphyry-style mineralization events: 480–475 Ma

and 470–460 Ma, respectively. Advanced tandem LA-ICP-MS/MS systems enable *in situ* Rb-Sr dating of white mica, which were used to determine the duration of magmatic-hydrothermal alteration of the Delamerian porphyry systems. Two temporal episodes are detected by the white mica Rb-Sr chronology: 480–460 Ma and 450 to 435 Ma. The first age interval is in accordance with the timing of intrusion emplacement and sulfide precipitation. The second interval likely records a regional thermal disturbance related to thermal activity in the adjacent Lachlan Orogen. Although *in situ* white mica Rb-Sr dating currently has poorer analytical precision than other presently more established chronologic analytical techniques, its advantages in easy, rapid sample preparation and isotopic measurement with high analytical output demonstrate great potential for dating magmatic-hydrothermal events within a variety of mineral deposits, where hydrothermal micas are common and widespread. Our zircon U-Pb, molybdenite Re-Os, and white mica Rb-Sr geochronology supports the Delamerian porphyry systems being a product of post-subduction processes, where fertile Cu-Mo fluids are ascribed to partial melting as a result of delamination or slab rollback induced asthenospheric upwelling. Our chronologic data indicate that porphyritic dikes and stocks with ages of 470–460 Ma are the most favorite exploration targets in the South Australian Delamerian Orogen.

Acknowledgements

This study is part of “Delamerian porphyry mineral systems” research project, supported by the Mineral Exploration Cooperative Research Centre (MinEx CRC, https://minexcrc.com.au/) whose activities are funded by the Australian Government's Cooperative Research Centre Program. This is MinEx CRC Document 2022/54. Geological Survey of South Australia provided additional funding and logistic support. Hyperspectral mineralogical data from drill cores sampled in this study are available via SARIG, https://map.sarig.sa.gov.au/. David Groom and Keryn Groom from South Australia Drill Hole Reference Library are thanked for their assistance during drill hole inspection. Aoife McFadden is acknowledged for assisting with BSE-CL and SEM-MLA imaging at Adelaide Microscopy. DS acknowledges technical support from Geoff Nowell and Chris Ottley of the Durham Geochemistry Centre. Ahmad Redaa, Darwinaji Subarkah, and Juraj Farkaš are thanked for helping Rb-Sr data reduction and interpretation. Rian Dutch and John Foden provided insightful discussion to improve this manuscript.

References

Aivazpourporgou, S., 2013, Lithospheric structures of the newer volcanics province, Western Victoria, Australia, from a long-period magnetotelluric method: Ph.D. thesis, Melbourne, Monash University, 158 p.

Alias, G., Sandiford, M., Hand, M., and Worley, B., 2002, The P–T record of synchronous magmatism, metamorphism and deformation at Petrel Cove, southern Adelaide Fold Belt: Journal of Metamorphic Geology, v. 20, p. 351-363.

Alva-Jimenez, T., Tosdal, R. M., Dilles, J. H., Dipple, G., Kent, A. J. R., and Halley, S., 2020, Chemical variations in hydrothermal white mica across the Highland Valley porphyry Cu-Mo district, British Columbia, Canada: Economic Geology, v. 115, p. 903-926.

Baatar, B., Parra-Avila, L. A., Fiorentini, M. L., Polito, P., and Crawford, A. J., 2020, Porphyry Cu fertility of the Loch Lilly-Kars Belt, Western New South Wales, Australia: Australian Journal of Earth Sciences, v. 67, p. 75-87.

Baker, J., Peate, D., Waight, T., and Meyzen, C., 2004, Pb isotopic analysis of standards and samples using a ^{207}Pb–^{204}Pb double spike and thallium to correct for mass bias with a double-focusing MC-ICP-MS: Chemical Geology, v. 211, p. 275-303.

Betts, M. J., Paterson, J. R., Jacquet, S. M., Andrew, A. S., Hall, P. A., Jago, J. B., Jagodzinski, E. A., Preiss, W. V., Crowley, J. L., Brougham, T., Mathewson, C. P., García-Bellido, D. C., Topper, T. P., Skovsted, C. B., and Brock, G. A., 2018, Early Cambrian chronostratigraphy and geochronology of South Australia: Earth-Science Reviews, v. 185, p. 498-543.

Blanckenburg, F. v., Villa, I., Baur, H., Morteani, G., and Steiger, R., 1989, Time calibration of a PT-path from the Western Tauern Window, Eastern Alps: the problem of closure temperatures: Contributions to Mineralogy and Petrology, v. 101, p. 1-11.

Boulesteix, T., Solé, J., Pi, T., and Cathelineau, M., 2020, Reappraisal of the GL-O reference material for K-Ar dating: New insight from microanalysis, single‐grain and milligram ar measurements: Geostandards and Geoanalytical Research, v. 44, p. 287-306.

Bowman, N., Van Otterloo, J., Cairns, C., Taylor, D., and Cas, R., 2019, Complex evolution of volcanic arcs: the lithofacies and palaeogeography of the Cambrian Stavely Arc, Delamerian Fold Belt, Western Victoria: Journal of Volcanology and Geothermal Research, v. 373, p. 120-132.

Cawood, P. A., 2005, Terra Australis Orogen: Rodinia breakup and development of the Pacific and Iapetus margins of Gondwana during the Neoproterozoic and Paleozoic: Earth-Science Reviews, v. 69, p. 249-279.

Cayley, R., 2011, Exotic crustal block accretion to the eastern Gondwanaland margin in the Late Cambrian–Tasmania, the Selwyn Block, and implications for the Cambrian–Silurian evolution of the Ross, Delamerian, and Lachlan orogens: Gondwana Research, v. 19, p. 628-649.

Chiaradia, M., Schaltegger, U., Spikings, R., Wotzlaw, J.-F., and Ovtcharova, M., 2013, How accutately can we date the duration of magmatic-hydrothemal events in porphyry systems?-An invited paper: Economic Geology, v. 108, p. 565-584.

Clifford, M., 2008, Drilling partnership – Netley Hill porphyry-style Cu-Mo mineral prospect – Project final report: Primary Industries and Resources SA, Government of South Australia, Open File Envelope No. 11576, 127 p.

Collins, W. J., 2002, Nature of extensional accretionary orogens: Tectonics, v. 21, p. 6-1–6-12.

Cooke, D. R., Hollings, P., Wilkinson, J. J., and Tosdal, R. M., 2014, Geochemistry of porphyry deposits: Treatise on Geochemistry 2nd ed., v. 13, p. 357-381.

Crawford, A., Meffre, S., Squire, R. J., Barron, L., and Falloon, T., 2007, Middle and Late Ordovician magmatic evolution of the Macquarie Arc, Lachlan Orogen, New South Wales: Australian Journal of Earth Sciences, v. 54, p. 181-214.

Curtis, S., 2020, Delamerian igneous basement to the Murray Basin in South Australia: A drill hole review – Volume 1: Department for Energy and Mining, Government of South Australia, Report Book 2020/00022, 261 p.

Duncan, R., Huston, D., Bastrakov, E., and Thomas, M., 2018, Known mineral occurrences in Stavely, *in* Schofield, A., ed., Regional geology and mineral systems of the Stavely Arc, western Victoria, Record 2018/02: Canberra, Geoscience Australia, p. 135-150.

Flöttmann, T., Haines, P., Jago, J., James, P., Belperio, A., and Gum, J., 1998, Formation and reactivation of the Cambrian Kanmantoo Trough, SE Australia: implications for early Palaeozoic tectonics at eastern Gondwana's plate margin: Journal of the Geological Society, v. 155, p. 525-539.

Foden, J., Elburg, M. A., Dougherty-Page, J., and Burtt, A., 2006, The timing and duration of the Delamerian Orogeny: correlation with the Ross Orogen and implications for Gondwana assembly: The Journal of Geology, v. 114, p. 189-210.

Foden, J., Elburg, M. A., Turner, S., Sandiford, M., O'Callaghan, J., and Mitchell, S., 2002, Granite production in the Delamerian orogen, South Australia: Journal of the Geological Society, v. 159, p. 557-575.

Foden, J., Elburg, M., Turner, S., Clark, C., Blades, M. L., Cox, G., Collins, A. S., Wolff, K., and George, C., 2020, Cambro-Ordovician magmatism in the Delamerian orogeny: Implications for tectonic development of the southern Gondwanan margin: Gondwana Research, v. 81, p. 490-521.

Foden, J., Sandiford, M., Dougherty-Page, J., and Williams, I., 1999, Geochemistry and geochronology of the Rathjen Gneiss: implications for the early tectonic evolution of the Delamerian Orogen: Australian Journal of Earth Sciences, v. 46, p. 377-389.

Forster, D., McInnes, P., Downes, P M., Maas, R., Norman, M., and Blevin, P.L., 2015, New lead isotopic and geochronologic constraints on mineralization in the Macquarie arc—insights from the Lake Cowal district, New South Wales: Geological Survey of New South Wales Quarterly Notes, August 2015, v. 144, p. 21.

Foster, D. A., and Gray, D. R., 2000, Evolution and structure of the Lachlan Fold Belt (Orogen) of Eastern Australia: Annual Review of Earth and Planetary Sciences, v. 28, p. 47-80.

Glen, R., Crawford, A., Percival, I., and Barron, L., 2007a, Early Ordovician development of the Macquarie Arc, Lachlan Orogen, New South Wales: Australian Journal of Earth Sciences, v. 54, p. 167-179.

Glen, R., Meffre, S., and Scott, R., 2007b, Benambran orogeny in the eastern Lachlan orogen, Australia: Australian Journal of Earth Sciences, v. 54, p. 385-415.

Greenfield, J. E., Musgrave, R. J., Bruce, M. C., Gilmore, P. J., and Mills, K. J., 2011, The Mount Wright Arc: A Cambrian subduction system developed on the continental margin of East Gondwana, Koonenberry Belt, eastern Australia: Gondwana Research, v. 19, p. 650-669.

Griessmann, M., 2011, Gold mineralisation in the Adelaide Fold Belt: Ph.D. thesis, Adelaide, The University of Adelaide, 201 p.

Haines, P. W., Turner, S. P., Foden, J. D., and Jago, J. B., 2009, Isotopic and geochemical characterisation of the Cambrian Kanmantoo Group, South Australia: implications for stratigraphy and provenance: Australian Journal of Earth Sciences, v. 56, p. 1095-1110.

Harris, A. C., Cooke, D. R., Cuison, A. L. G., Groome, M., Wilson, A. J., Fox, N., Holliday, J., and Tosdal, R. M., 2020, Geologic evolution of late Ordovician to early Silurian alkalic porphyry Au-Cu deposits at Cadia, New South Wales: SEG Special Publications, v. 23, p. 621–643.

Hogmalm, K. J., Zack, T., Karlsson, A. K.-O., Sjöqvist, A. S., and Garbe-Schönberg, D., 2017, In situ Rb–Sr and K–Ca dating by LA-ICP-MS/MS: an evaluation of N_2O and SF_6 as reaction gases: Journal of Analytical Atomic Spectrometry, v. 32, p. 305-313.

Hoskin, P. W. O., and Schaltegger, U., 2003, The composition of zircon and igneous and metamorphic petrogenesis: Reviews in Mineralogy and Geochemistry, v. 53, p. 27-62.

Hosking, A. J., 1970, Netley Hill progress and final reports to licence expiry/Surrender for the Period 1/12/1986 to 30/11/1969: Primary Industries and Resources SA, Government of South Australia, Open File Envelop No. 1088, 126 p.

Jackson, S. E., Pearson, N. J., Griffin, W. L., and Belousova, E. A., 2004, The application of laser ablation-inductively coupled plasma-mass spectrometry to in situ U–Pb zircon geochronology: Chemical geology, v. 211, p. 47-69.

Jago, J. B., Gum, J., Burtt, A., and Haines, P. W., 2003, Stratigraphy of the Kanmantoo Group: A critical element of the Adelaide Fold Belt and the Palaeo-Pacific plate margin, Eastern Gondwana: Australian Journal of Earth Sciences, v. 50, p. 343-363.

Johnson, E. L., Phillips, G., and Allen, C. M., 2016, Ediacaran–Cambrian basin evolution in the Koonenberry Belt (eastern Australia): Implications for the geodynamics of the Delamerian Orogen: Gondwana Research, v. 37, p. 266-284.

Kemp, A. I. S., Hawkesworth, C. J., Collins, W. J., Gray, C. M., and Blevin, P. L., 2009, Isotopic evidence for rapid continental growth in an extensional accretionary orogen: The Tasmanides, eastern Australia: Earth and Planetary Science Letters, v. 284, p. 455-466.

Kemp, A., 2003, Plutonic boninite-like rocks in an anatectic setting: Tectonic implications for the Delamerian orogen in southeastern Australia: Geology, v. 31, p. 371-374.

Langsford, N. R., 1971, The investigation of the Bendigo copper and molybdenum prospect – Report No. 1. Report Book 71/129: Department of Mines, South Australia., 62 p.

Langsford, N. R., 1973, The investigation of the Bendigo copper and molybdenum prospect – Report No. 4 – Diamond drilling. Report Book 73/63: Department of Mines, South Australia., 33 p.

Lawley, C. J. M., and Selby, D., 2012, Re-Os geochronology of quartz-enclosed ultrafine molybdenite: implications for ore geochronology: Economic Geology, v. 107, p. 1499-1505.

Leslie, C., Meffre, S., Cooke, D. R., Thompson, J., Howard, N., and Barker, A., 2021, Complex petrogenesis of porphyry-related magmas in the Cowal district, Australia: Insights from LA ICP-MS zircon imaging: SEG Special Publications, v. 24, Tectonomagmatic influences on metallogeny and hydrothermal ore deposits: A tribute to Jeremy P. Richards (Volume II), p. 159–180.

Li, Y., Selby, D., Condon, D., and Tapster, S., 2017, Cyclic magmatic-hydrothermal evolution in porphyry systems: High-precision U-Pb and Re-Os geochronology constraints on the Tibetan Qulong Porphyry Cu-Mo deposit: Economic Geology, v. 112, p. 1419-1440.

Lickfold, V., Cooke, D. R., Smith, S. G., and Ullrich, T. D., 2003, Endeavour copper-gold porphyry deposits, Northparkes, New South Wales: intrusive history and fluid evolution: Economic Geology, v. 98, p. 1607-1636.

Lloyd, J. C., Blades, M. L., Counts, J. W., Collins, A. S., Amos, K. J., Wade, B. P., Hall, J. W., Hore, S., Ball, A. L., Shahin, S., and Drabsch, M., 2020, Neoproterozoic geochronology and provenance of the Adelaide Superbasin: Precambrian Research, v. 350, 105849, 29 p.

Lloyd, J. C., Collins, A. S., Blades, M. L., Gilbert, S. E., and Amos, K. J., 2022, Early evolution of the Adelaide Superbasin: Geosciences, v. 12, 154, 28 p.

Marshak, S., and Flöttmann, T., 1996, Structure and origin of the Fleurieu and Nackara Arcs in the Adelaide fold-thrust belt, South Australia: salient and recess development in the Delamerian Orogen: Journal of Structural Geology, v. 18, p. 891-908.

McDonald, G. D., 1992, The petrology and timing of the Anabama Granite and associated igneous activity, Olary region, S.A.: B.Sc. (Honours) thesis, Adelaide, The University of Adelaide, 40 p.

Meffre, S., Scott, R., Glen, R., and Squire, R. J., 2007, Re-evaluation of contact relationships between Ordovician volcanic belts and the quartz-rich turbidites of the Lachlan Orogen: Australian Journal of Earth Sciences, v. 54, p. 363-383.

Merdith, A. S., Williams, S. E., Collins, A. S., Tetley, M. G., Mulder, J. A., Blades, M. L., Young, A., Armistead, S. E., Cannon, J., and Zahirovic, S., 2021, Extending full-plate tectonic models into deep time: Linking the Neoproterozoic and the Phanerozoic: Earth-Science Reviews, v. 214, p. 103477.

Morris, B. J., 1977, An investigation of copper and molybdenum mineralization at Anabama Hill and the Cronje Dam copper prospect: Department of Mines, South Australia, Open File Envelope No. 03054, 155 p.

Nakamura, A., and Milligan, P. R., 2015, Total Magnetic Intensity (TMI) Grid of Australia 2015 - sixth edition, Geoscience Australia.

Nasev, N. A., 1998, The use of zircon inheritance and isotopic composition in the recognition of the source of the Cambro-Ordovician granites of the Adelaide Fold Thrust Belt, South Australia: B.Sc. (Honours) thesis, Adelaide, University of Adelaide, 90 p.

Pollard, P. J., Jongens, R., Stein, H., Mark Fanning, C., and Smillie, R., 2021, Rapid formation of porphyry and skarn copper-gold Mineralization in a postsubduction environment: Re-Os and U-Pb geochronology of the Ok Tedi Mine, Papua New Guinea: Economic Geology, v. 116, p. 533-558.

Pollock, M. V., Spry, P. G., Tott, K. A., Koenig, A., Both, R. A., and Ogierman, J., 2018, The origin of the sediment-hosted Kanmantoo Cu-Au deposit, South Australia: Mineralogical considerations: Ore Geology Reviews, v. 95, p. 94-117.

Preiss, W., 2000, The Adelaide Geosyncline of South Australia and its significance in Neoproterozoic continental reconstruction: Precambrian Research, v. 100, p. 21-63.

Rattigan, J. H., Tonkin, D. G., Wilson, P. D., Burlinson, K., Stokoe, G. C., Hellman, P. L., Fountain, R. J., and Miller, P. G., 1982, Anabama Hill progress reports and final report to licence expiry/full surrender, for the period 7/11/1980 to 6/11/1982: Department of Mines and Energy, South Australia, Open File Envelope No. 04029, 114 p.

Redaa, A., Farkaš, J., Gilbert, S., Collins, A. S., Wade, B., Löhr, S., Zack, T., and Garbe-Schönberg, D., 2021, Assessment of elemental fractionation and matrix effects during in situ Rb–Sr dating of phlogopite by LA-ICP-MS/MS: implications for the accuracy and precision of mineral ages: Journal of Analytical Atomic Spectrometry, v. 36, p. 322-344.

Redaa, A., Farkaš, J., Hassan, A., Collins, A. S., Gilbert, S., and Löhr, S. C., 2022, Constraints from in-situ Rb-Sr dating on the timing of tectono-thermal events in the Umm Farwah shear zone and associated Cu-Au mineralisation in the Southern Arabian Shield, Saudi Arabia: Journal of Asian Earth Sciences, v. 224, p. 105037.

Reid, A., Forster, M., Preiss, W., Caruso, A., Curtis, S., Wise, T., Vasegh, D., Goswami, N., and Lister, G., 2022, Complex $^{40}Ar/^{39}Ar$ age spectra from low-grade metamorphic rocks: resolving the input of detrital and metamorphic components in a case study from the Delamerian Orogen: Geochronology, https://doi.org/10.5194/gchron-2021-41.

Richards, J. P., 2009, Postsubduction porphyry Cu-Au and epithermal Au deposits: Products of remelting of subduction-modified lithosphere: Geology, v. 37, p. 247-250.

Richards, J. P., and Mumin, A. H., 2013, Magmatic-hydrothermal processes within an evolving Earth: Iron oxide-copper-gold and porphyry Cu ± Mo ± Au deposits: Geology, v. 41, p. 767-770.

Robertson, K., Taylor, D., Thiel, S., and Heinson, G., 2015, Magnetotelluric evidence for serpentinisation in a Cambrian subduction zone beneath the Delamerian Orogen, southeast Australia: Gondwana Research, v. 28, p. 601-611.

Rockwell Resources and Kelpie Exploration, 2017, Sherlock - Annual reports: Department of the Premier and Cabinet, Government of South Australia, Open File Envelope No. 11877, 399 p.

Romer, R. L., and Smeds, S.-A., 1996, U–Pb columbite ages of pegmatites from Sveconorwegian terranes in southwestern Sweden: Precambrian Research, v. 76, p. 15-30.

Rush, J.A., 2013, Geology of the Marsden Cu-Au Porphyry, NSW: B.Sc. (Honours) thesis, Hobart, University of Tasmania, 110 p.

Schofield, A., 2018, Regional geology and mineral systems of the Stavely Arc, western Victoria: Record 2018/02, Geoscience Australia, Canberra, 220 p, http://dx.doi.org/10.11636/Record.2018.002.

Seedorff, E., Dilles, J. H., Proffett, J. M., Einaudi, M. T., Zurcher, L., Stavast, W. J., Johnson, D. A., and Barton, M. D., 2005, Porphyry deposits: Characteristics and origin of hypogene features: Economic Geology 100th Anniversary Volume, p. 251-298.

Seymour, D. B., Green, G. R., and Calver, C. R., 2007, The geological and mineral deposits of Tasmania: a summary: Tasmanian Geological Survey Bulletin 72, p. 1-29.

Sinclair, W. D., 2007, Porphyry deposits, *in* Goodfellow, W. D., ed., Mineral Deposits of Canada: A synthesis of Mjor deposit-types, District Metallogeny, the Evolution of Geological provinces, and Exploration

Methods, Special Publication No.5, Geological Association of Canada, Mineral Deposits Division, p. 223-243.

Sláma, J., Košler, J., Condon, D. J., Crowley, J. L., Gerdes, A., Hanchar, J. M., Horstwood, M. S., Morris, G. A., Nasdala, L., and Norberg, N., 2008, Plešovice zircon—a new natural reference material for U–Pb and Hf isotopic microanalysis: Chemical Geology, v. 249, p. 1-35.

Smoliar, M. I., Walker, R. J., and Morgan, J. W., 1996, Re-Os ages of group IIA, IIIA, IVA, and IVB iron meteorites: Science, v. 271, p. 1099-1102.

Stavely Minerals, 2022. The Stavely copper-gold project – Dawn of a new world-class copper-gold province in Western Victoria: MRE presentation, June 2022, 31 p.

Subarkah, D., Blades, M. L., Collins, A. S., Farkaš, J., Gilbert, S., Löhr, S. C., Redaa, A., Cassidy, E., and Zack, T., 2022, Unraveling the histories of Proterozoic shales through in situ Rb-Sr dating and trace element laser ablation analysis: Geology, v. 50, p. 66-70.

Tott, K. A., Spry, P. G., Pollock, M. V., Koenig, A., Both, R. A., and Ogierman, J., 2019, Ferromagnesian silicates and oxides as vectors to metamorphosed sediment-hosted Pb-Zn-Ag-(Cu-Au) deposits in the Cambrian Kanmantoo Group, South Australia: Journal of Geochemical Exploration, v. 200, p. 112-138.

Turner, S., Foden, J., and Morrison, R., 1992, Derivation of some A-type magmas by fractionation of basaltic magma: an example from the Padthaway Ridge, South Australia: Lithos, v. 28, p. 151-179.

Vermeesch, P., 2018, IsoplotR: A free and open toolbox for geochronology: Geoscience Frontiers, v. 9, p. 1479-1493.

Villa, I. M., De Bièvre, P., Holden, N., and Renne, P., 2015, IUPAC-IUGS recommendation on the half life of ^{87}Rb: Geochimica et Cosmochimica Acta, v. 164, p. 382-385.

Wiedenbeck, M., Alle, P., Corfu, F., Griffin, W., Meier, M., Oberli, F., Quadt, A. v., Roddick, J., and Spiegel, W., 1995, Three natural zircon standards for U-Th-Pb, Lu-Hf, trace element and REE analyses: Geostandards newsletter, v. 19, p. 1-23.

Wilson, A. J., R., C. D., Stein, H. J., Fanning, C. M., Holliday, J. R., and Tedder, I. J., 2007, U-Pb and Re-Os geochronologic evidence for two alkalic porphyry ore-forming events in the Cadia district, New South Wales, Australia: Economic Geology, v. 102, p. 3-26.

Zack, T., and Hogmalm, K. J., 2016, Laser ablation Rb/Sr dating by online chemical separation of Rb and Sr in an oxygen-filled reaction cell: Chemical Geology, v. 437, p. 120-133.

Zukowski, W., 2010, Geology and mineralization of the Endeavour 41 gold deposit, Cowal district, NSW, Australia: Ph.D. thesis, Hobart, University of Tasmania, 287 p.

Figure captions:

Fig. 1. (A) Orogenic belts of eastern Australia (after Foden et al., 2020). (B) Geologic elements of the Delamerian Orogen in South Australia, Victorian, and New South Wales, overlain on the total magnetic intensity (TMI) grid of eastern Australia (Nakamura and Milligan, 2015). Highlighted are the associated magmatic – hydrothermal ore deposits and occurrences within the studied region, including porphyry Cu-Mo mineralized prospects discussed herein.

Fig. 2. Sketch geologic maps for Delamerian porphyry prospects highlighting studied drill hole sites. (A) Anabama Hill, adapted from McDonald (1992). (B) Netley Hill, adapted from Hosking (1970). (C) Bendigo, adapted from Langsford (1973).

Fig. 3. Photograph showing granitoids and hydrothermal alteration features at Anabama Hill. (A) Anabama granodiorite cut by pyrite-quartz vein with weakly pervasive chlorite alteration, from 136 m (DDHAN7). Note that biotite aggregates define an aligned lineation oblique to the long axis of drill core. (B) Intrusive contacts of the granodiorite and plagioclase-phyric diorite at Anabama Hill, from 79 to 90 m (DDHAN7). (C) Granodiorite enclaves contained in the plagioclase-phyric diorite at 93 m (DDHAN7). (D) Discontinuous, thin K-feldspar veinlets (K1 vein) cutting the porphyritic diorite with Pl-phenocrysts at 563.2 m (DDHAN7). (E) K-feldspar-phyric dike intruding chlorite-epidote-muscovite-pyrite altered granodiorite; the porphyritic dike cut by multiple sets of narrow pyrite-quartz-muscovite vein (W3). (F) Coarse-grained muscovite-pyrite-quartz vein (W1) cutting the monzogranite from DDHAN7 at 744 m. (G) Epidote-chlorite vein (P1) superimposing early K-feldspar vein (K2), both cutting the granodiorite. (H) Massive muscovite-pyrite-quartz alteration (W3 vein) overprinting epidote-chlorite-altered granodiorite at a depth of 197.7 m (ANDDH6). (I) Coarse-grained chalcopyrite associated with pyrite-quartz-muscovite-quartz-magnetite veins (W2) cutting the granodiorite at 220.1 m (AHDDH4). Abbreviations: Ccp = chalcopyrite, Py = pyrite, Chl = chlorite, Ep = epidote, Kfs = K-feldspar, Pl = plagioclase, Mag = magnetite, Ms = muscovite, Qtz = quartz.

Fig. 4. Photograph showing hydrothermal alteration features at Netley Hill. (A) Discontinuous thin K-feldspar-quartz-biotite ± pyrite vein (2-3 mm wide; K1 vein) cut the granodiorite, from 94.5m (NTDD001). (B) Three veining stages occur in the plagioclase-pyric diorite. Early pale K-feldspar vein (K2 vein) is truncated by distinctive gray muscovite-magnetite ± quartz vein (W1 vein), and a later thick quartz vein (1-10 cm wide; W3 vein) with centerlines of pyrite ± chalcopyrite (D vein) grow along the early K-feldspar vein and cut both the K-feldspar vein and muscovite-magnetite vein (NTDD003, 336 m). (C) Crosscutting muscovite-magnetite-quartz veins have centerline of pyrite ± chalcopyrite (W1 vein) and overprint the K-feldspar-altered granodiorite at 162.6 m (NTDD003). (D) Thick gray to greenish muscovite-quartz vein (2-3 cm wide) contains a centerline of magnetite ± pyrite (W2 vein), cutting a red porphyry at 199 m (NTDD002). (E) Coarse-grained chalcopyrite intergrown with quartz as clots within the red porphyry (NTDD002, 240.4 m). (F) Pyrite-chalcopyrite-quartz vein with gray muscovite halos (W1 vein) extend along the boundary between red porphyry stock and biotite-phyric granite at 273 m (NTDD002). (G) Molybdenite grains filled along fractures in massive gray muscovite-quartz-pyrite vein with width up to 5 cm (W4 vein), cutting red fine-grained aplite (NTDD001, 192.5 m). Abbreviations: Bi = biotite, Ccp = chalcopyrite, Py = pyrite, Moly = molybdenite, Kfs = K-feldspar, Pl = plagioclase, Mag = magnetite, Ms = muscovite, Qtz = quartz.

Fig. 5. Photograph showing hydrothermal alteration features at Bendigo. (A) Planar quartz-pyrite ± molybdenite veins with K-feldspar halos (K2 vein) in the granodiorite (BD2, 96.5 m). (B) Banded molybdenite-quartz-pyrite ± chalcopyrite veins with thin K-feldspar halos (BQM vein; BD3, 190 m). (C) Greenish muscovite-quartz-molybdenite ± chalcopyrite vein (W1) overprints the quartz-pyrite vein with thin K-feldspar halos (K2 vein). (D) Thick pyrite-quartz vein (>5 cm wide) contains coarse-grained molybdenite, cutting the intense argillically altered granite (BD5, 112.2 m). (E) Chlorite ± epidote veins (P1) in the granodiorite (BD4, 138.5 m). (F) Quartz-pyrite veins with thin K-feldspar halos (K3) cutting plagioclase-phyric diorite dike (BD4, 126.2 m). (G) Plagioclase-phenocrysts selectively altered to be epidote-chlorite assemblage in the diorite dike (BD7, 176.7 m). (H) Sheeted quartz-pyrite-chalcopyrite vein cuts K-feldspar-altered porphyritic diorite (BD7, 176.8 m). (I) Planar quartz-magnetite-pyrite ± chalcopyrite veins with thick pale greenish muscovite-quartz-pyrite envelopes (W2 vein) cutting medium-grained granite (BD3, 96.5 m). Abbreviations: Ccp = chalcopyrite, Moly = molybdenite, Py = pyrite, Chl = chlorite, Ep = epidote, Kfs = K-feldspar, Mag = magnetite, Ms = muscovite, Pl = plagioclase, Qtz = quartz.

Fig. 6. Geology and mineralogy in the Colebatch prospect. (A) Equigranular granite consisting of quartz, K-feldspar, and minor biotite and chlorite. (B) Coarse-grained molybdenite in a thick quartz vein cutting the Colebatch granite.

Fig. 7. Representative mineral liberation analysis (MLA) images highlighting mineralogical and textural features of magmatic-hydrothermal alteration in the Delamerian porphyry systems. Anabama Hill: (A) Quartz-white mica overprinting epidote-chlorite alteration in granodiorite, (B) Epidote-pyrite ± chalcopyrite vein cutting white mica-chlorite altered diorite, and (C) White mica-pyrite-chalcopyrite vein cutting K-feldspar altered monzogranite. Netley Hill: (D) White mica-quartz cemented breccias with albite-altered clasts, (E) Massive quartz-white mica alteration in porphyritic diorite, and (F) Pyrite-quartz vein cutting the granite with intense white mica alteration and disseminated chalcopyrite. Bendigo: (G) Fine-grained diorite having strong albite and moderate white mica alteration, (H) Thick white mica-pyrite-chalcopyrite vein cutting albite-bearing granite, and (I) Massive white mica-quartz alteration on the granodiorite.

Fig. 8. Cathodoluminescence features of representative zircons for Delamerian granitic intrusions. Anabama Hill: (A) Granodiorite, (B) Diorite, (C) Monzogranite, and (D) Porphyritic dacite. Netley Hill: (E) Granodiorite, (F) Diorite, (G) Biotite granite, and (H) Red K-feldspar granite. Bendigo: (I) Granodiorite, (J) Biotite granite,

and (K) Porphyritic diorite. (L) Colebatch granite. Red circles represent LA-ICP-MS analytical spots, and related $^{206}Pb/^{238}U$ ages are annotated.

Fig. 9. Zircon U-Pb Wetherill diagrams for granitoids from the Anabama Hill porphyry prospects. (A) Granodiorite, (B) diorite dike, (C) monzogranite, and (D) porphyritic dacite dike. Weighted mean ages, host lithologies, and sample numbers are labelled in the diagrams. Non-filled ellipses are not included for Concordia or weighted average $^{206}Pb/^{238}U$ age calculation. Insets in each Concordia are weighted mean plots for each pluton. Gray bars are $^{206}Pb/^{238}U$ ages with 2σ uncertainty with decay constant.

Fig. 10. Zircon U-Pb Wetherill diagrams for granitoids from the Netley Hill porphyry prospect. (A) Granodiorite, (B) red K-feldspar granite, (C) diorite dike, and (D) biotite-phyric granite. Labels and legends similar to Figure 9.

Fig. 11. Zircon U-Pb Wetherill diagrams for granitoids from Bendigo and Colebatch prospects. Bendigo: (A) granodiorite, (B) biotite granite, and (C) diorite dike. (D) Colebatch granite. Labels and legends similar to Figure 9.

Fig. 12. Rb-Sr isochrons for white mica from the Anabama Hill prospect. Isochron ages, regressed initial Sr isotopic values, and sample numbers are annotated in the plots. All ellipses represent 95% confidence intervals.

Fig. 13. Rb-Sr isochrons for white mica from the Netley Hill prospect. Labels and legends similar to Figure 12.

Fig. 14. Rb-Sr isochrons for white mica from the Bendigo prospect. Labels and legends similar to Figure 12.

Fig. 15. Combined chronological data showing the temporal framework of the Delamerian porphyry Cu-Mo mineral systems (this study) with that of the Delamerian Orogeny (Foden et al., 2006), in comparison to porphyry Cu deposits in the Macquarie Arc of Lachlan Orogen. $^{40}Ar/^{39}Ar$ ages of metasediments from Reid et al. (2022). Zircon U-Pb and molybdenite Re-Os ages for porphyry Cu-Au deposits in the Cadia Valley and Cowal Lake districts, NSW from Wilson et al. (2007), Zukowski (2010), Rush (2013), Foster et al. (2015), and Harris et al. (2020) and references therein. Molybdenite Re-Os age of 459.7 ± 1.4 Ma and older zircon populations (458–455 Ma) from Wilson et al. (2007) at Cadia Quarry were reinterpreted to be unreliable by Harris et al. (2020). Abbreviations: Ms = muscovite, Qtz = quartz, Moly = molybdenite, Py = pyrite, PCD = porphyry Cu deposits.

Fig. 16. Schematic cartoons showing evolution of metallogenic settings in the Delamerian Orogen and adjacent regions. (A) Subduction, deformation, and magmatism in the Delamerian Orogen from 520 to 490 Ma, accompanied with I- and S-type granitoid emplacement in South Australia and porphyry Cu formation (505–498 Ma) in the Victorian Stavley Arc (modified from Richards, 2009; Schofield, 2018; Foden et al., 2020). (B) Post-tectonic magmatism from 490 to 470 Ma represented by extensive A-type granitoid intrusion in South Australia, followed by post-subduction porphyry Cu-Mo mineralization within the Delamerian continental margin (e.g., Anabama Hill, Netley Hill, and Bendigo; 470–460 Ma) that formed simultaneously with the earliest-known porphyry mineralization (467–455 Ma) in the intraoceanic Macquarie Arc (modified from Glen et al., 2007a; Richards, 2009; Schofield, 2018; Foden et al., 2020).

Figure 1

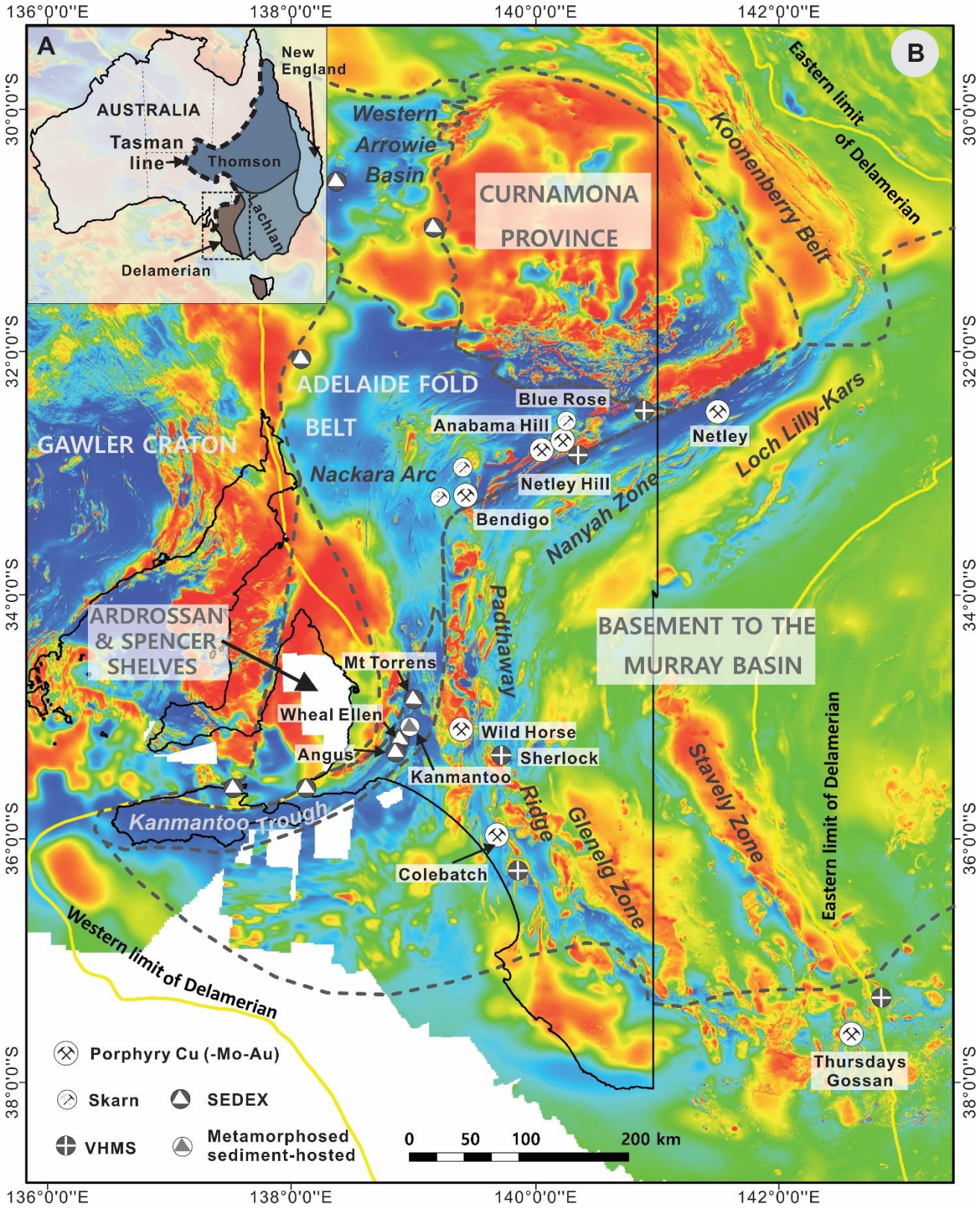
A
AUSTRALIA
New England
Tasman line
Thomson
Lachlan
Delamerian
B
Western Arrowie Basin
CURNAMONA PROVINCE
Koonenberry Belt
Eastern limit of Delamerian
ADELAIDE FOLD BELT
GAWLER CRATON
Nackara Arc
Blue Rose
Anabama Hill
Netley
Netley Hill
Bendigo
Loch Lilly-Kars
Nanyah Zone
Padthaway Ridge
ARDROSSAN & SPENCER SHELVES
BASEMENT TO THE MURRAY BASIN
Mt Torrens
Wheal Ellen
Angus
Wild Horse
Sherlock
Kanmantoo
Kanmantoo Trough
Colebatch
Glenelg Zone
Stavely Zone
Eastern limit of Delamerian
Western limit of Delamerian
Thursdays Gossan
Porphyry Cu (-Mo-Au)
Skarn
SEDEX
VHMS
Metamorphosed sediment-hosted
0 50 100 200 km
136°0'0"E
138°0'0"E
140°0'0"E
142°0'0"E
30°0'0"S
32°0'0"S
34°0'0"S
36°0'0"S
38°0'0"S

Figure 2

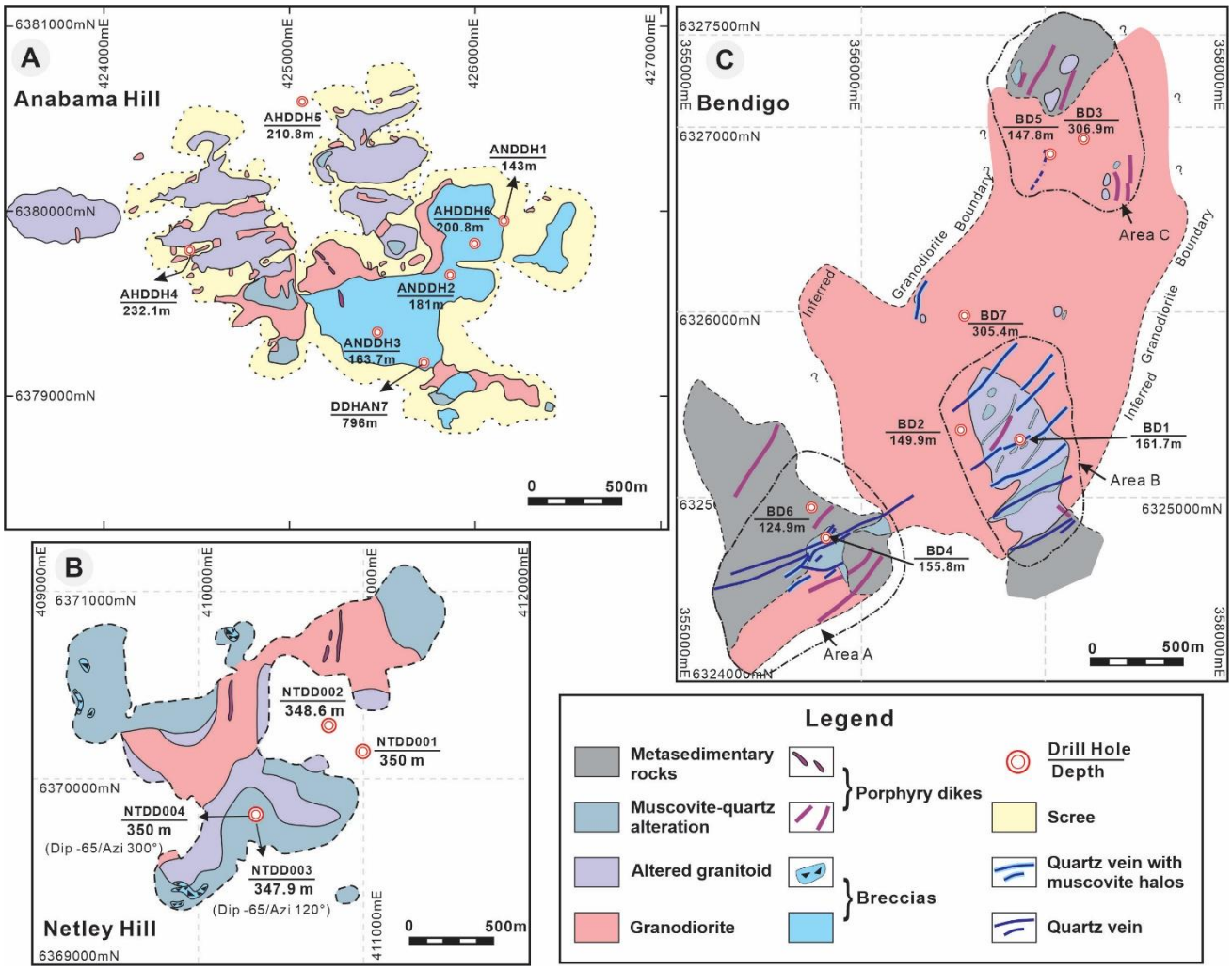
A
Anabama Hill
6381000mN
6380000mN
6379000mN
424000mE
425000mE
426000mE
427000mE
AHDDH5
210.8m
ANDDH1
143m
AHDDH6
200.8m
AHDDH4
232.1m
ANDDH2
181m
ANDDH3
163.7m
DDHAN7
796m
0
500m
B
Netley Hill
6371000mN
6370000mN
6369000mN
409000mE
410000mE
411000mE
412000mE
NTDD002
348.6 m
NTDD001
350 m
NTDD004
350 m
(Dip -65/Azi 300°)
NTDD003
347.9 m
(Dip -65/Azi 120°)
0
500m
C
Bendigo
6327500mN
6327000mN
6326000mN
6325000mN
6324000mN
355000mE
356000mE
358000mE
BD5
147.8m
BD3
306.9m
Area C
Granodiorite Boundary
Inferred
BD7
305.4m
BD2
149.9m
BD1
161.7m
Area B
BD6
124.9m
BD4
155.8m
Area A
0
500m
Legend
Metasedimentary rocks
Muscovite-quartz alteration
Altered granitoid
Granodiorite
Porphyry dikes
Breccias
Drill Hole
Depth
Scree
Quartz vein with muscovite halos
Quartz vein

Figure 3

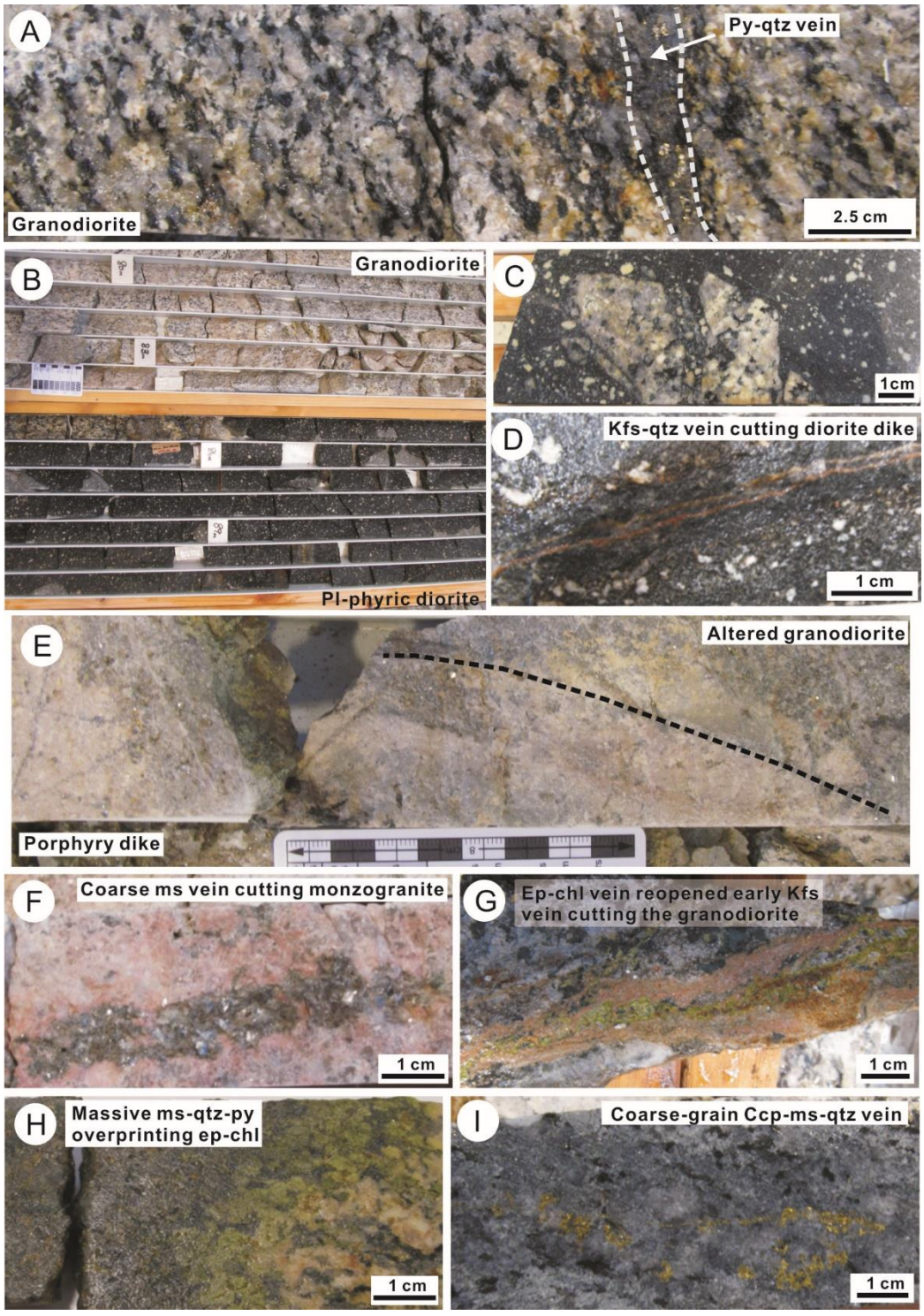
A
Py-qtz vein
Granodiorite
2.5 cm
B
Granodiorite
Pl-phyric diorite
C
1cm
D
Kfs-qtz vein cutting diorite dike
1 cm
E
Altered granodiorite
Porphyry dike
F
Coarse ms vein cutting monzogranite
1 cm
G
Ep-chl vein reopened early Kfs vein cutting the granodiorite
1 cm
H
Massive ms-qtz-py overprinting ep-chl
1 cm
I
Coarse-grain Ccp-ms-qtz vein
1 cm

Figure 4

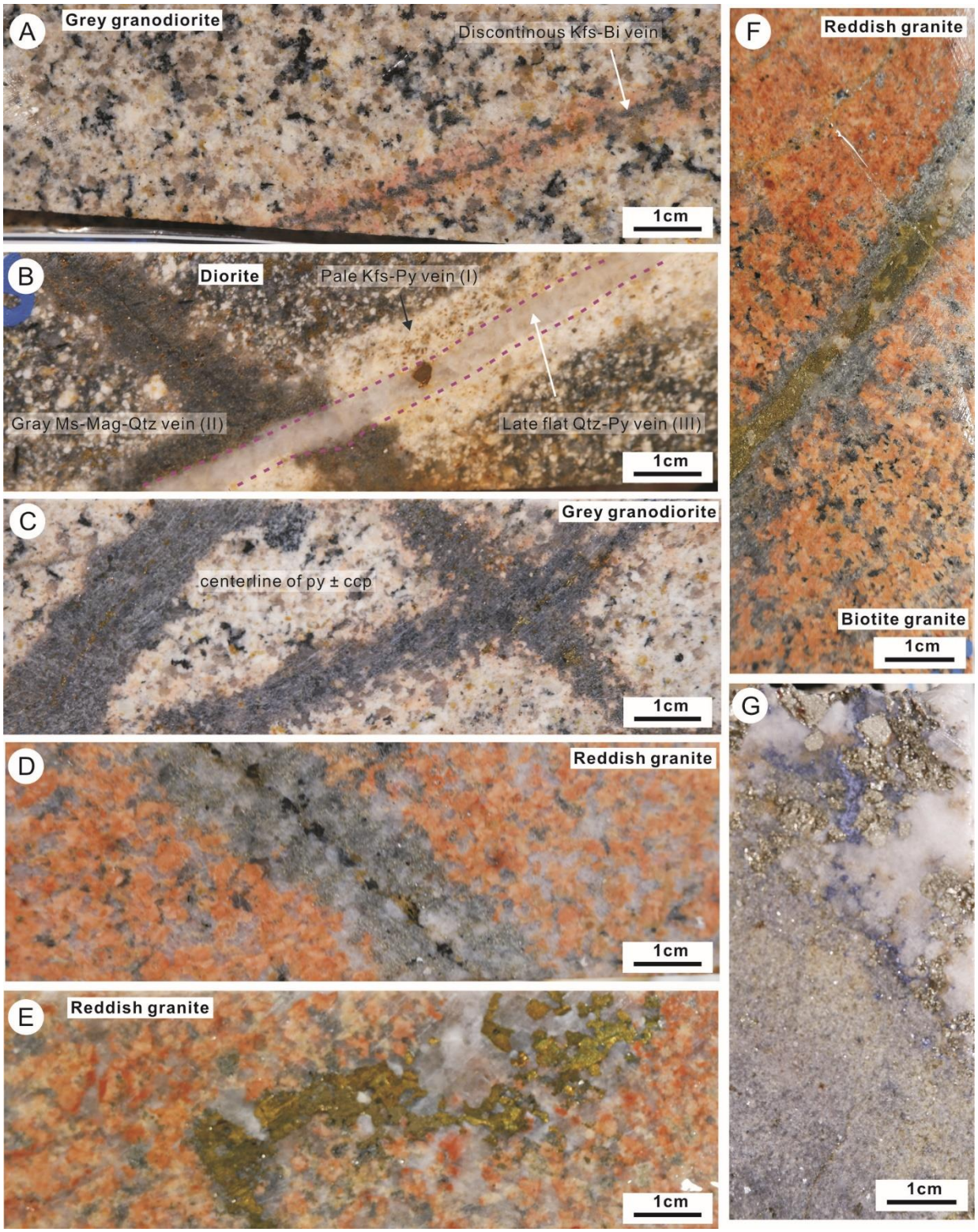
A
Grey granodiorite
Discontinous Kfs-Bi vein
1cm
B
Diorite
Pale Kfs-Py vein (I)
Gray Ms-Mag-Qtz vein (II)
Late flat Qtz-Py vein (III)
1cm
C
Grey granodiorite
centerline of py ± ccp
1cm
D
Reddish granite
1cm
E
Reddish granite
1cm
F
Reddish granite
Biotite granite
1cm
G
1cm

Figure 5

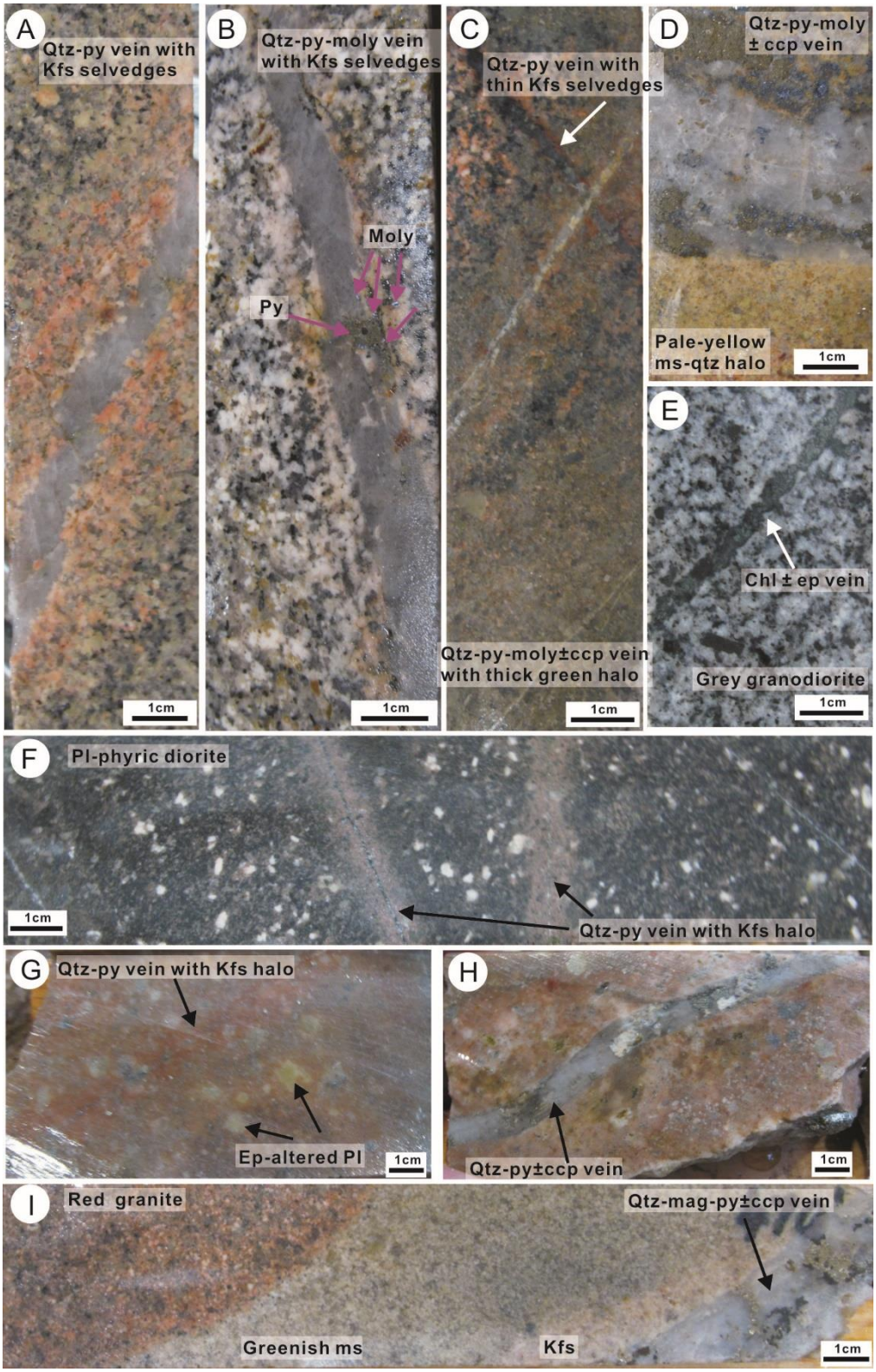
A
Qtz-py vein with Kfs selvedges
1cm
B
Qtz-py-moly vein with Kfs selvedges
Moly
Py
1cm
C
Qtz-py vein with thin Kfs selvedges
Qtz-py-moly±ccp vein with thick green halo
1cm
D
Qtz-py-moly ± ccp vein
Pale-yellow ms-qtz halo
1cm
E
Chl ± ep vein
Grey granodiorite
1cm
F
Pl-phyric diorite
1cm
Qtz-py vein with Kfs halo
G
Qtz-py vein with Kfs halo
Ep-altered Pl
1cm
H
Qtz-py±ccp vein
1cm
I
Red granite
Qtz-mag-py±ccp vein
Greenish ms
Kfs
1cm

Figure 6

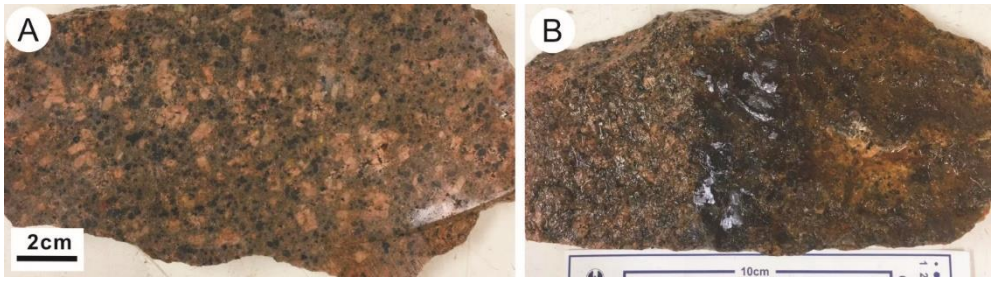

Figure 7

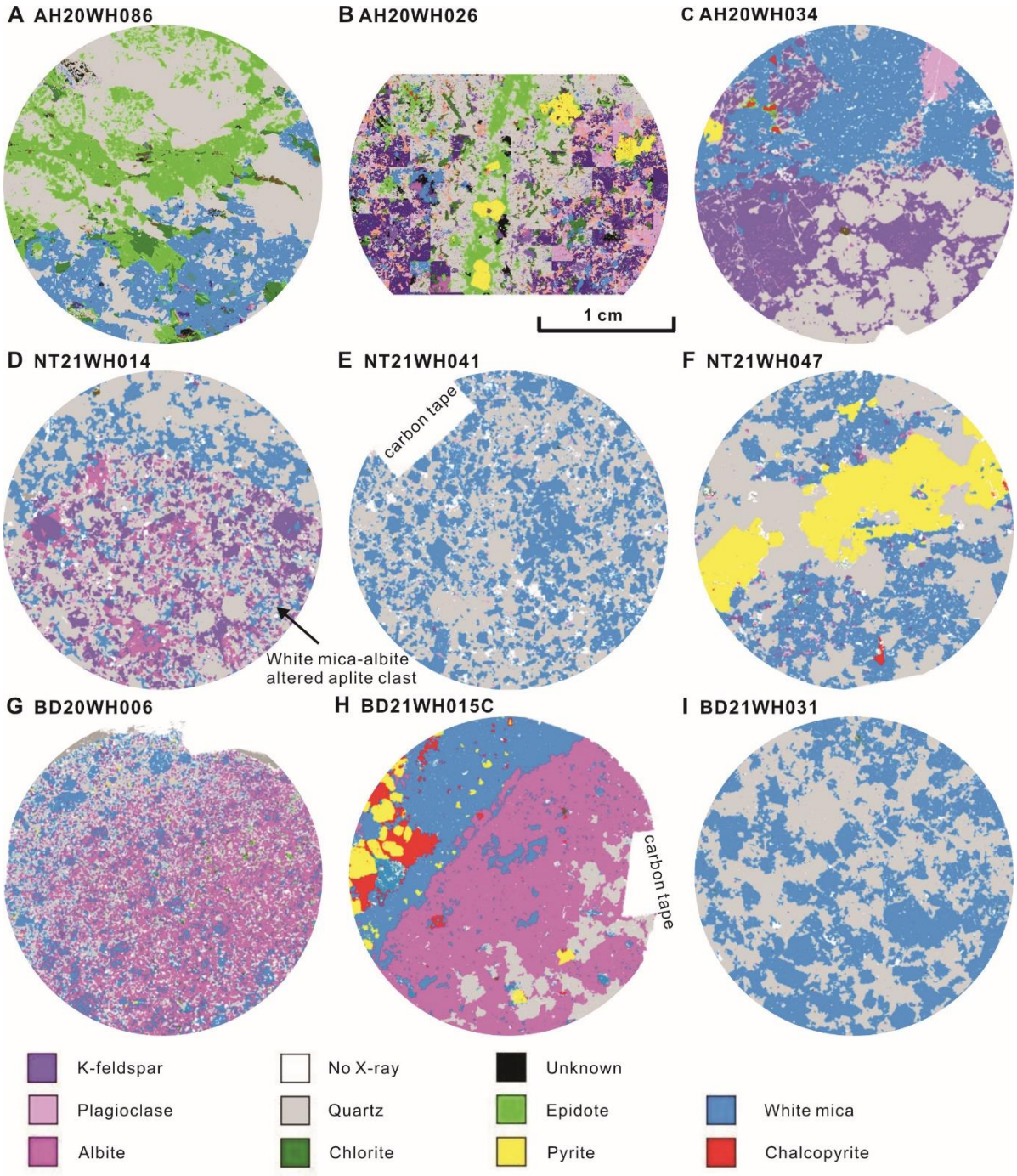

Figure 8

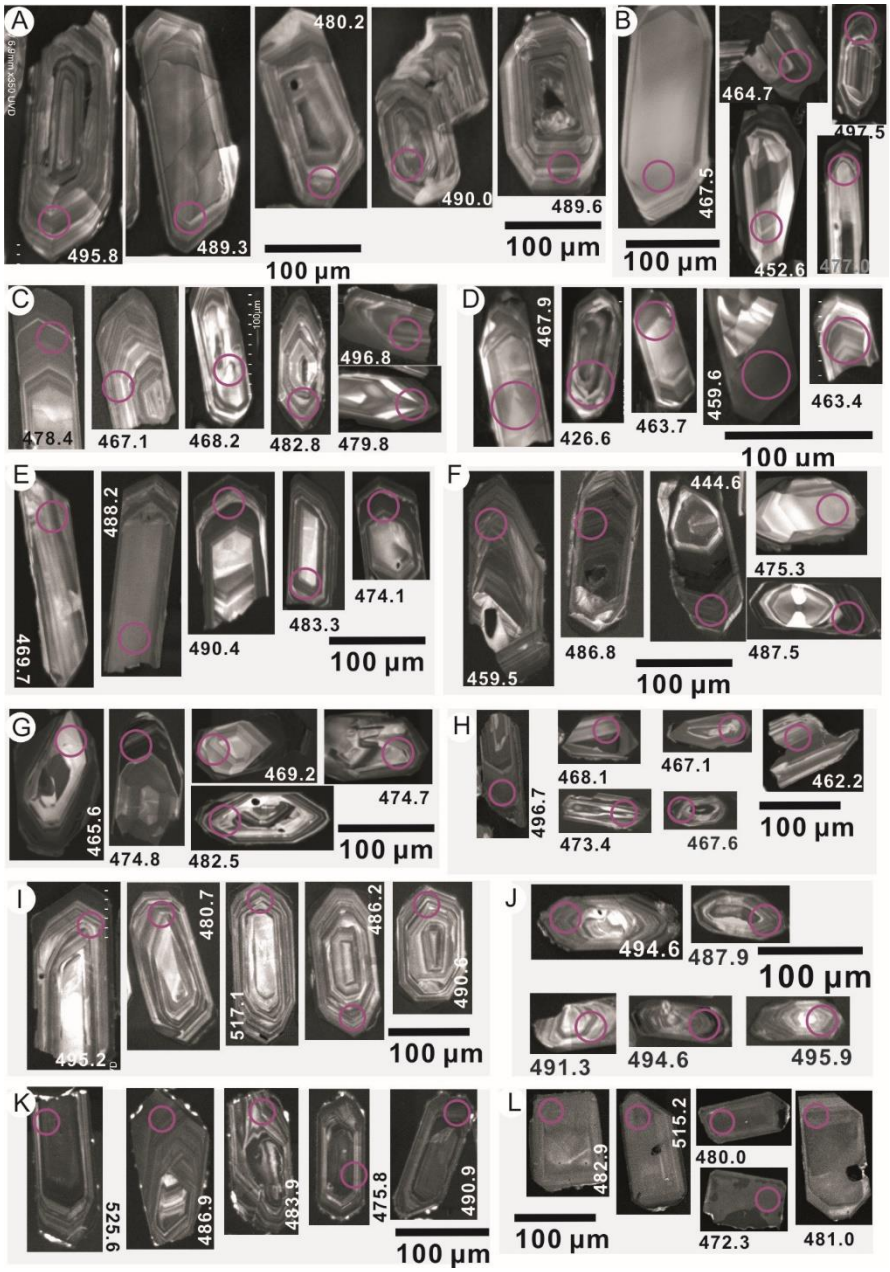
A
495.8
489.3
480.2
490.0
489.6
100 µm
B
467.5
464.7
452.6
497.5
100 µm
C
478.4
467.1
468.2
482.8
496.8
479.8
D
467.9
426.6
463.7
459.6
463.4
100 µm
E
469.7
488.2
490.4
483.3
474.1
100 µm
F
459.5
486.8
444.6
475.3
487.5
100 µm
G
465.6
474.8
482.5
469.2
474.7
100 µm
H
496.7
468.1
473.4
467.1
467.6
462.2
100 µm
I
495.2
480.7
517.1
486.2
490.8
100 µm
J
494.6
487.9
491.3
494.6
495.9
100 µm
K
523.6
486.9
483.9
475.8
490.9
100 µm
L
482.9
515.2
480.0
472.3
481.0
100 µm

Figure 9

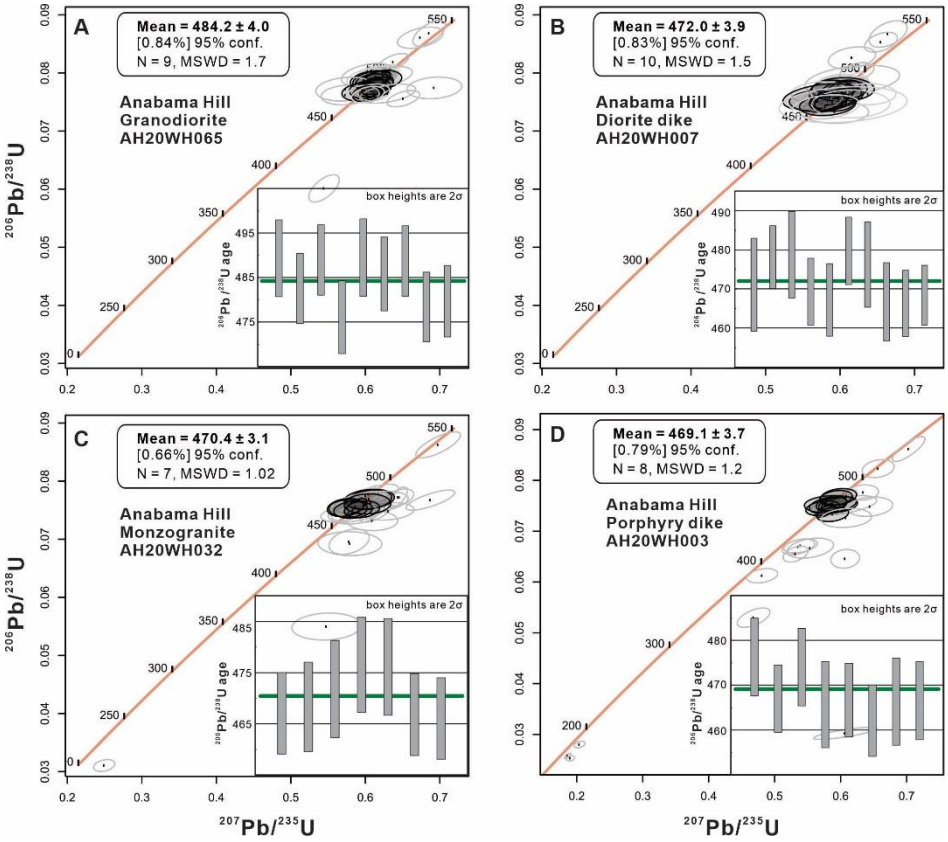

Figure 10

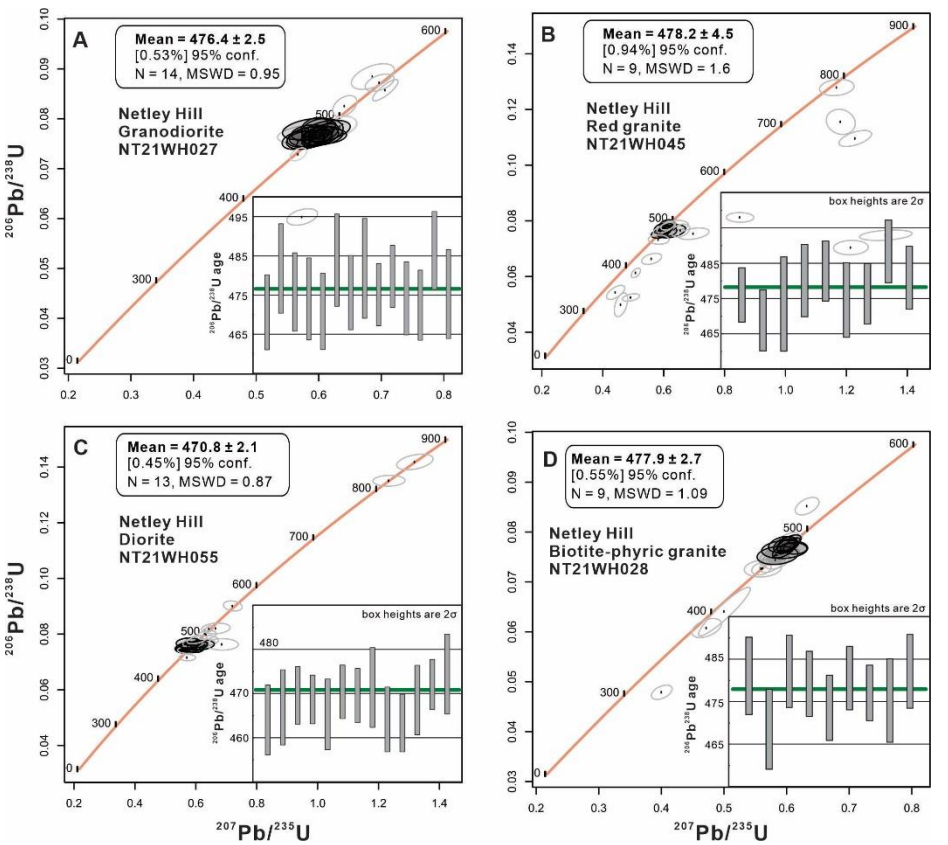

Figure 11

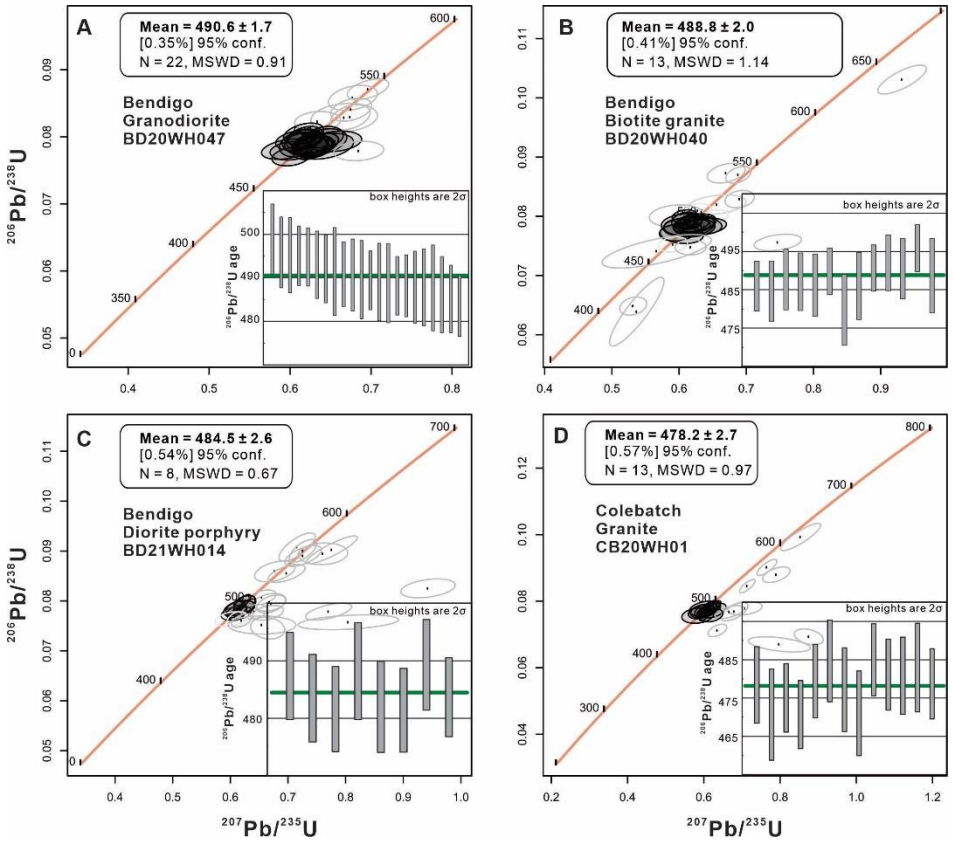
A
Mean = 490.6 ± 1.7
[0.35%] 95% conf.
N = 22, MSWD = 0.91
Bendigo
Granodiorite
BD20WH047
box heights are 2σ
B
Mean = 488.8 ± 2.0
[0.41%] 95% conf.
N = 13, MSWD = 1.14
Bendigo
Biotite granite
BD20WH040
box heights are 2σ
C
Mean = 484.5 ± 2.6
[0.54%] 95% conf.
N = 8, MSWD = 0.67
Bendigo
Diorite porphyry
BD21WH014
box heights are 2σ
D
Mean = 478.2 ± 2.7
[0.57%] 95% conf.
N = 13, MSWD = 0.97
Colebatch
Granite
CB20WH01
box heights are 2σ
206Pb/238U
207Pb/235U
207Pb/235U age

Figure 12

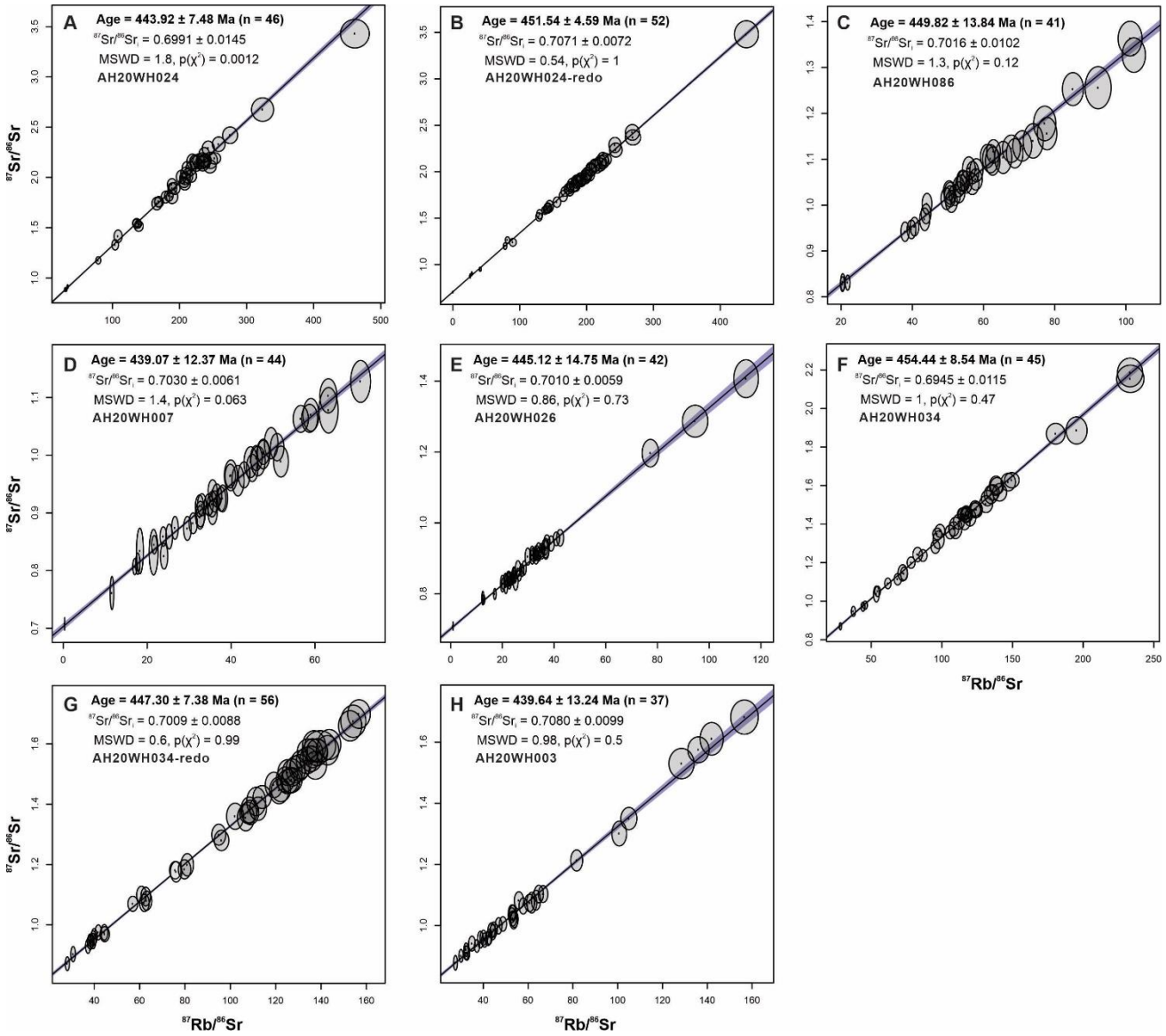
A
Age = 443.92 ± 7.48 Ma (n = 46)
87Sr/86Sri = 0.6991 ± 0.0145
MSWD = 1.8, p(χ2) = 0.0012
AH20WH024
B
Age = 451.54 ± 4.59 Ma (n = 52)
87Sr/86Sri = 0.7071 ± 0.0072
MSWD = 0.54, p(χ2) = 1
AH20WH024-redo
C
Age = 449.82 ± 13.84 Ma (n = 41)
87Sr/86Sri = 0.7016 ± 0.0102
MSWD = 1.3, p(χ2) = 0.12
AH20WH086
D
Age = 439.07 ± 12.37 Ma (n = 44)
87Sr/86Sri = 0.7030 ± 0.0061
MSWD = 1.4, p(χ2) = 0.063
AH20WH007
E
Age = 445.12 ± 14.75 Ma (n = 42)
87Sr/86Sri = 0.7010 ± 0.0059
MSWD = 0.86, p(χ2) = 0.73
AH20WH026
F
Age = 454.44 ± 8.54 Ma (n = 45)
87Sr/86Sri = 0.6945 ± 0.0115
MSWD = 1, p(χ2) = 0.47
AH20WH034
G
Age = 447.30 ± 7.38 Ma (n = 56)
87Sr/86Sri = 0.7009 ± 0.0088
MSWD = 0.6, p(χ2) = 0.99
AH20WH034-redo
H
Age = 439.64 ± 13.24 Ma (n = 37)
87Sr/86Sri = 0.7080 ± 0.0099
MSWD = 0.98, p(χ2) = 0.5
AH20WH003
87Sr/86Sr
87Rb/86Sr

Figure 13

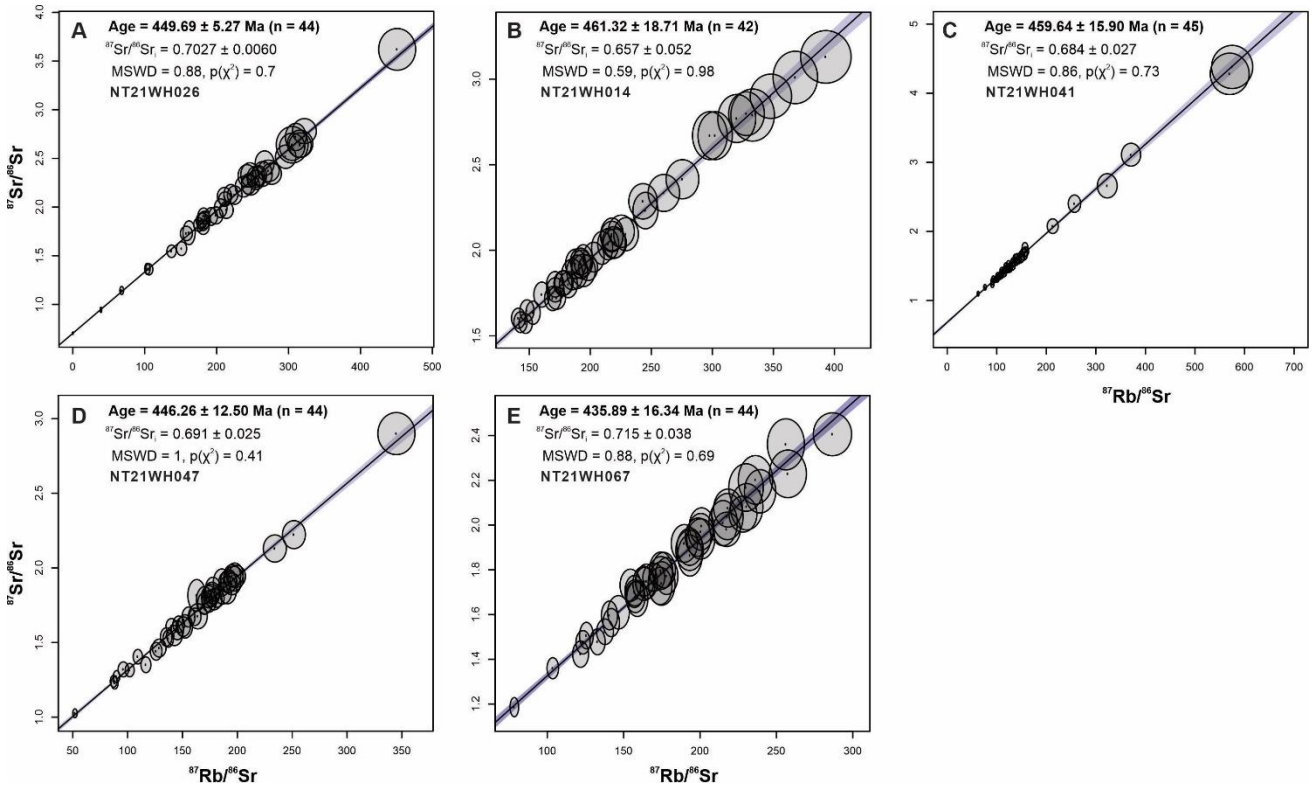

Figure 14

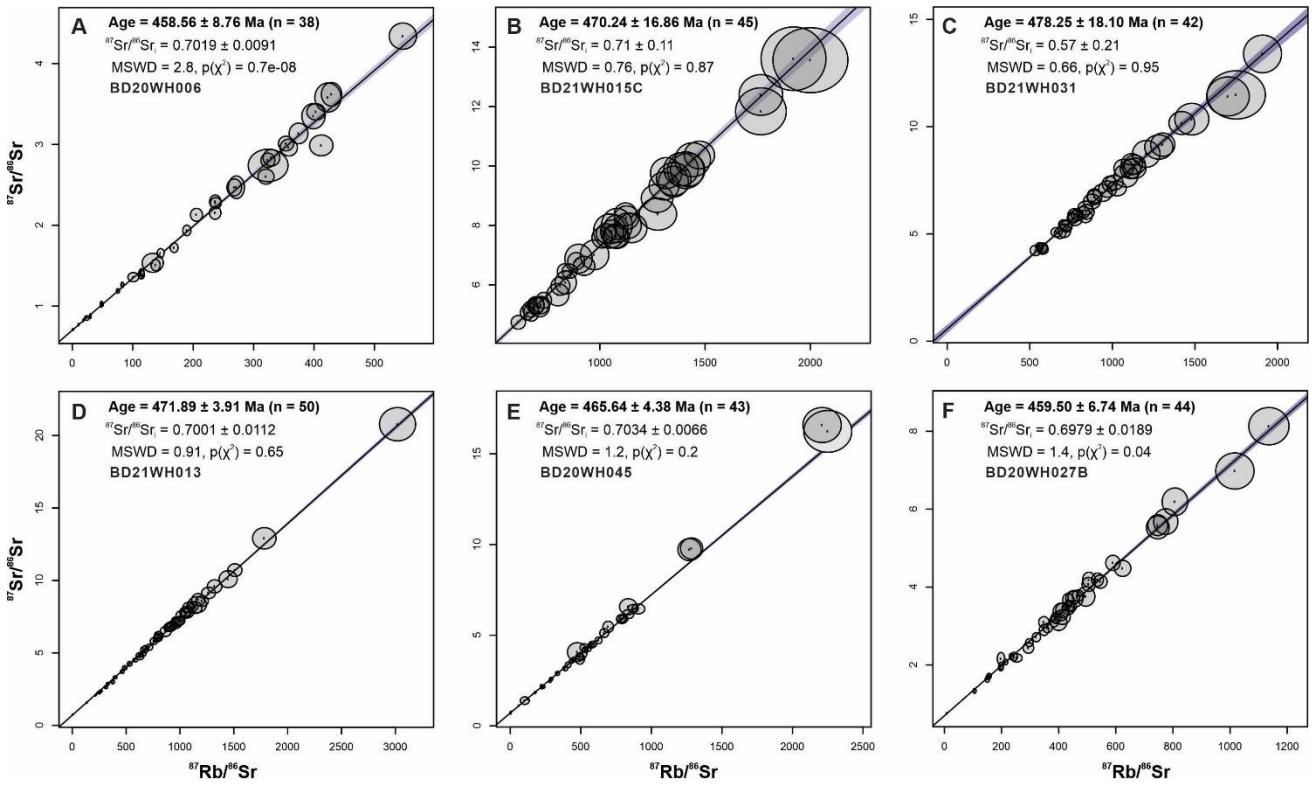

Figure 15

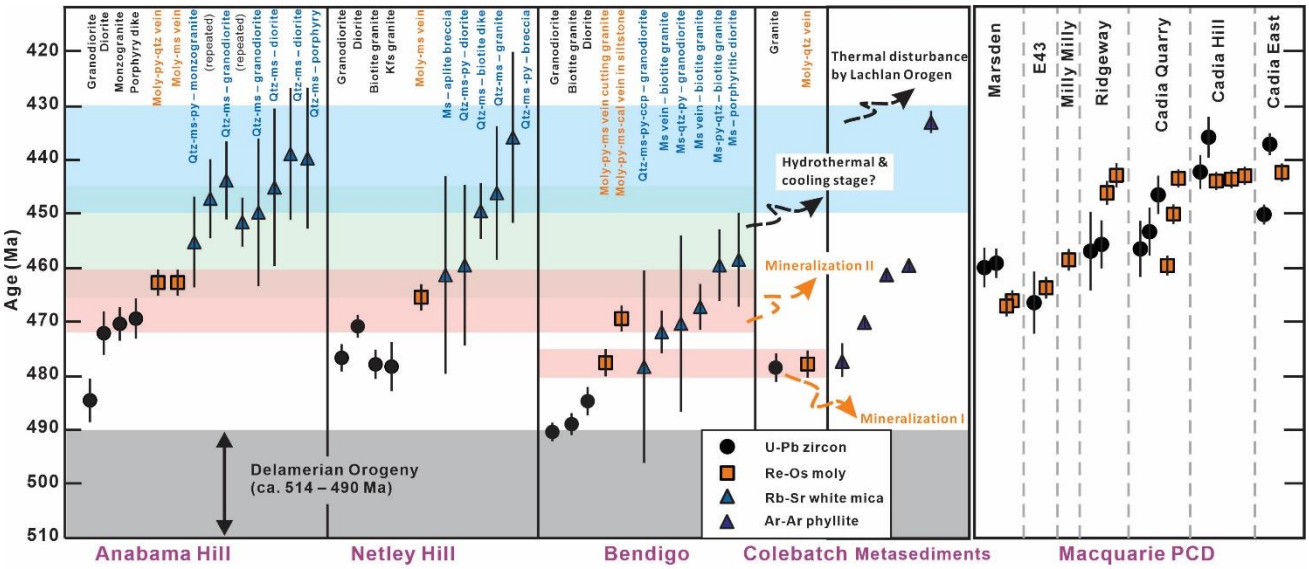

Figure 16

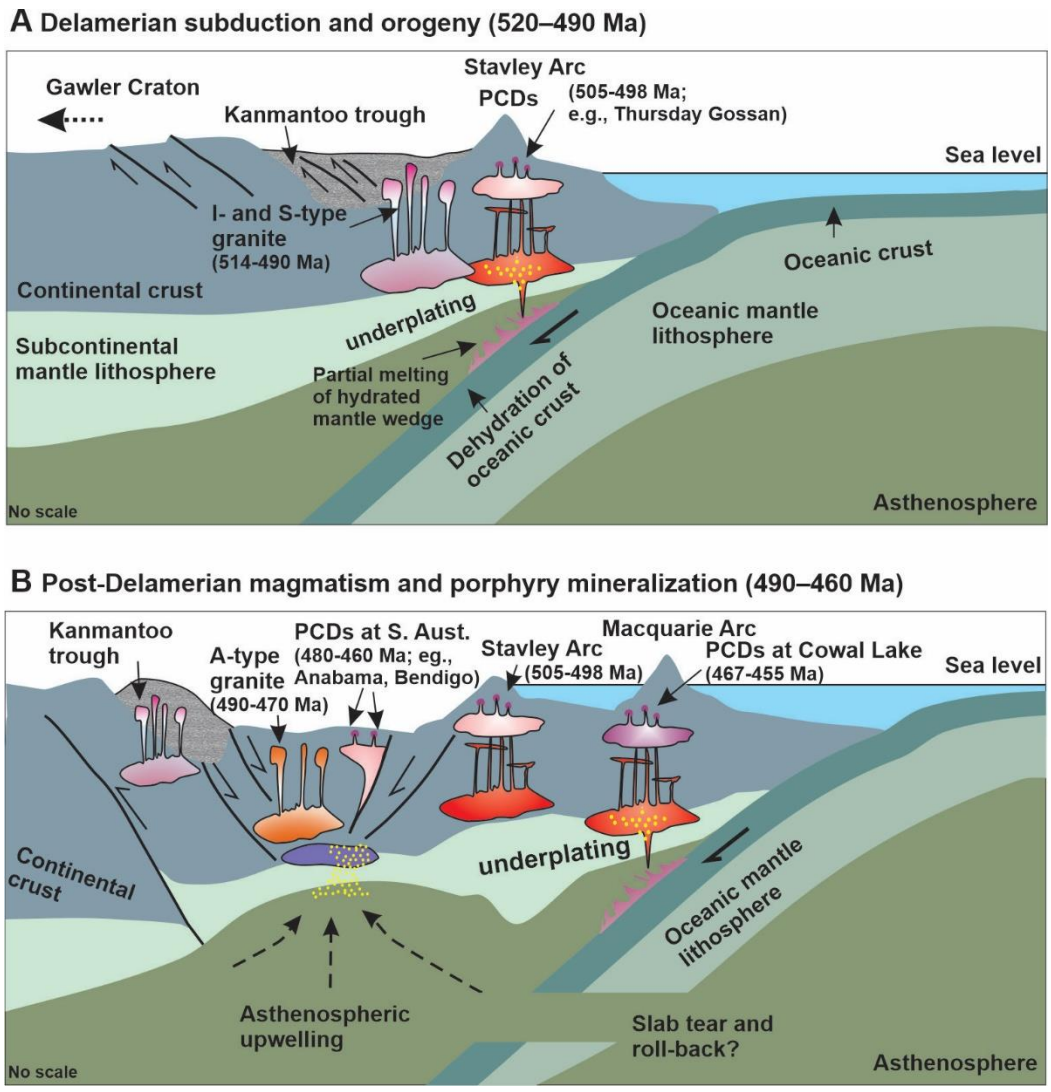

Table 1. Summary of main features of the porphyry Cu-Mo prospects from the Delamerian Orogen

Prospect	Coordinates	Intrusive rocks	Alteration characteristics	Vein classification	Country rocks
Anabama Hill	E140°10' – E140°16', S32°41' – S32°45'	Granodiorite, plagioclase-phyric diorite, monzogranite, and Kfs-phyric porphyry	Weak potassic (K-feldspar) alteration; moderate epidote-chlorite-rich propylitic alteration; widespread phyllic alteration dominated by muscovite-pyrite-quartz assemblage; capped by a 50 m-thick weathering zone consisting of kaolinite, montmorillonite, jarosite, and goethite	K1: discontinuous kfs-qtz veinlet (n mm wide) K2: granular kfs veinlet (up to 1 cm wide) P1: chl-ep ± ab ± py ± ccp vein P2: ep-qtz-mag-py ±ccp ± moly vein W1: green to dark ms-qtz ± py ± ccp ± moly vein W2: ms-qtz-mag-py ± coarse ccp vein W3: qtz-py-moly vein (> 1 m wide) with thick ms halos	Neoproterozoic Umberatana Group of mica schists, tillites, quartzites, and siltstones
Netley Hill	E140°02' – E140°05', S32°47' – S32°50'	Granodiorite, porphyritic diorite, biotite-phyric granite, red K-feldspar granite, aplite	Quartz-pyrite ± chalcopyrite veinlets and veins selvaged by K-feldspar halos; minor discontinuous K-feldspar-quartz ± biotite veins; pervasive muscovite-pyrite-quartz vein-type alteration overprint earlier potassic alteration; weak to moderate chlorite and epidote alteration replaces feldspar and/or biotite in the granitoids and rare narrow chlorite-quartz vein	K1: thin qtz-bi ± py ± ccp vein with kfs halos K2: pale kfs vein ± py ± ccp vein BMQ: sheeted moly-qtz-py vein W1: thick qtz-ms-py vein (1-10 cm wide) W2: pale to green ms-qtz-mag-py ± ccp vein W3: massive qtz-rich vein (10 cm wide) with py ± ccp	Neoproterozoic Umberatana Group of tillites, quartzites, siltstones, and slates
Bendigo	E139°23' – E139°23', S33°09' – S33°15'	Granodiorite, biotite granite, porphyritic diorite, and minor dacite porphyritic dikes	Common quartz-pyrite ± magnetite ± chalcopyrite ± bornite ± molybdenite veins with thin K-feldspar ± biotite selvedges; widespread muscovite-quartz-pyrite alteration, and additional epidote-chlorite vein-type and selective alteration; reddish K-feldspar-quartz ± sulfide veins locally cut the granitoids; chalcopyrite and bornite inclusions are typically hosted in pyrite	K1: discontinuous kfs-qtz ± bi ± py vein K2: thick qtz-py ± moly vein with kfs halos K3: thin bi-qtz ± py veinlet with kfs envelops BMQ: banded moly-qtz-py ± ccp vein P: thin chl ± ep vein W1: qtz-py ± ccp ± moly vein with thick ms-qtz ± cal halos W2: planar qtz ± mag-py ± bn vein with ms-qtz-py CQ: cal-qtz-py-moly ± ccp vein and/or veinlet	Neoproterozoic sequences of mica schists, tillites, quartzites, and siltstones
Colebatch	E139°46'5", S35°53'42"	Granite	Selectively weak chlorite-muscovite alteration and 5 mm-1cm wide molybdenite-quartz vein	moly-qtz ± chl vein	Not available

Ab = albite, bi = biotite, cal = calcite, chl = chlorite, ep = epidote, kfs = K-feldspar, ms = muscovite, qtz = quartz, bn = bornite, ccp = chalcopyrite, py = pyrite, moly = molybdenite, mag = magnetite

Table 2. Re-Os isotopic compositions and ages for molybdenite samples from the Delamerian porphyry Cu-Mo prospects

Sample ID	Prospect	Rock description	weight (g)	Re (ppm)	±	^{187}Re (ppm)	±	^{187}Os (ppb)	±	Age (Ma)	±^	±*	±#
AH20WH014	Anabama Hill	Disseminated molybdenite grains with muscovite cut thick quartz-pyrite vein (> 10 cm wide)	0.020	44.65	0.17	28.06	0.11	217.2	0.69	462.9	0.3	1.9	2.4
AH20WH062	Anabama Hill	Massive quartz vein contains coarse-grained pyrite and muscovite, and fine-grained, disseminated molybdenite	0.020	31.29	0.12	19.67	0.07	152.2	0.49	462.7	0.3	1.9	2.4
NT21WH039	Netley Hill	Molybdenite-pyrite-quartz vein cuts red fine-grained porphyritic aplite	0.015	191.0	0.79	120.1	0.50	934.8	3.39	465.6	0.3	1.9	2.4
BD21WH027	Bendigo	5 cm wide molybdenite-pyrite-quartz vein cutting intensely altered granite	0.021	55.3	0.21	34.7	0.13	277.5	0.87	477.7	0.4	1.9	2.5
BD21WH033	Bendigo	Molybdenite-pyrite-quartz-carbonate vein, with a width of 0.5–1 cm, cutting dark siltstone	0.010	385.3	1.94	242.2	1.22	1901.4	8.79	469.4	0.3	1.9	2.4
CB20WH01	Colebatch	Coase-grained molybdenite vein (0.5–1 cm wide) cuts the Colebatch Granite	0.068	10.08	0.03	6.33	0.02	50.6	0.13	477.9	0.3	2.0	2.5

^uncertainty including only mass spectrometry uncertainty;
*uncertainty including all sources of analytical uncertainty;
#uncertainty including all sources of analytical uncertainty and decay constant.

Table 3. Combined geochronological data for the Delamerian porphyry prospects from this study

Sample ID	Prospect	Mineral	Dating method	Age (Ma)	±* (Ma)	±# (Ma)	$^{87}Sr/^{86}Sr_{initial}$
AH20WH065	Anabama Hill	Zircon	LA-ICP-MS, U-Pb	484.2	2.7	4.0	
AH20WH007	Anabama Hill	Zircon	LA-ICP-MS, U-Pb	472.0	2.9	3.9	
AH20WH032	Anabama Hill	Zircon	LA-ICP-MS, U-Pb	470.4	3.1	3.2	
AH20WH003	Anabama Hill	Zircon	LA-ICP-MS, U-Pb	469.1	2.9	3.7	
AH20WH014	Anabama Hill	Molybdenite	ID-NTIMS, Re-Os	462.9	1.9	2.4	
AH20WH062	Anabama Hill	Molybdenite	ID-NTIMS, Re-Os	462.7	1.9	2.4	
AH20WH007	Anabama Hill	White mica	LA-ICP-MS/MS, Rb-Sr	439.1		12.4	0.7030 ± 0.0061
AH20WH003	Anabama Hill	White mica	LA-ICP-MS/MS, Rb-Sr	439.6		13.2	0.7080 ± 0.0099
AH20WH024	Anabama Hill	White mica	LA-ICP-MS/MS, Rb-Sr	443.9		7.5	0.6991 ± 0.0145
AH20WH024redo	Anabama Hill	White mica	LA-ICP-MS/MS, Rb-Sr	451.5		4.6	0.7071 ± 0.0072
AH20WH026	Anabama Hill	White mica	LA-ICP-MS/MS, Rb-Sr	445.1		14.8	0.7010 ± 0.0059
AH20WH086	Anabama Hill	White mica	LA-ICP-MS/MS, Rb-Sr	449.8		13.8	0.7016 ± 0.0102
AH20WH034A	Anabama Hill	White mica	LA-ICP-MS/MS, Rb-Sr	454.4		8.5	0.6945 ± 0.0115
AH20WH034redo	Anabama Hill	White mica	LA-ICP-MS/MS, Rb-Sr	447.3		7.4	0.7009 ± 0.0088
NT21WH027	Netley Hill	Zircon	LA-ICP-MS, U-Pb	476.6	2.7	2.7	
NT21WH045	Netley Hill	Zircon	LA-ICP-MS, U-Pb	478.2	3.0	4.5	
NT21WH055	Netley Hill	Zircon	LA-ICP-MS, U-Pb	470.8	2.1	2.2	
NT21WH028	Netley Hill	Zircon	LA-ICP-MS, U-Pb	477.9	2.7	3.5	
NT21WH039	Netley Hill	Molybdenite	ID-NTIMS, Re-Os	465.6	1.9	2.4	
NT21WH014	Netley Hill	White mica	LA-ICP-MS/MS, Rb-Sr	461.3		18.7	0.6570 ± 0.052
NT21WH026	Netley Hill	White mica	LA-ICP-MS/MS, Rb-Sr	449.6		5.3	0.7027 ± 0.0031
NT21WH041	Netley Hill	White mica	LA-ICP-MS/MS, Rb-Sr	459.6		15.9	0.6840 ± 0.027
NT21WH047	Netley Hill	White mica	LA-ICP-MS/MS, Rb-Sr	446.3		12.5	0.6910 ± 0.025
NT21WH067	Netley Hill	White mica	LA-ICP-MS/MS, Rb-Sr	435.9		16.3	0.7150 ± 0.038
BD20WH047	Bendigo	Zircon	LA-ICP-MS, U-Pb	490.6	1.7	1.7	
BD20WH040	Bendigo	Zircon	LA-ICP-MS, U-Pb	488.8	2.0	2.0	
BD21WH014	Bendigo	Zircon	LA-ICP-MS, U-Pb	484.5	2.6	2.7	
BD21WH027	Bendigo	Molybdenite	ID-NTIMS, Re-Os	477.7	1.9	2.5	
BD21WH033	Bendigo	Molybdenite	ID-NTIMS, Re-Os	469.4	1.9	2.4	
BD20WH027B	Bendigo	White mica	LA-ICP-MS/MS, Rb-Sr	459.5		6.7	0.6979 ± 0.0189
BD21WH031	Bendigo	White mica	LA-ICP-MS/MS, Rb-Sr	478.3		18.1	0.57 ± 0.21
BD21WH015C	Bendigo	White mica	LA-ICP-MS/MS, Rb-Sr	470.2		16.9	0.71 ± 0.22
BD20WH006	Bendigo	White mica	LA-ICP-MS/MS, Rb-Sr	458.6		8.8	0.7019 ± 0.0091
BD20WH045	Bendigo	White mica	LA-ICP-MS/MS, Rb-Sr	465.6		4.4	0.7034 ± 0.0066
BD21WH013	Bendigo	White mica	LA-ICP-MS/MS, Rb-Sr	471.9		3.9	0.7001 ± 0.0112
CB20WH02	Colebatch	Zircon	LA-ICP-MS, U-Pb	478.2	2.7	2.8	
CB20WH01	Colebatch	Molybdenite	ID-NTIMS, Re-Os	477.9	2.0	2.5	

*Uncertainty including 2σ level of analytical uncertainty.
Uncertainty including 2σ level of analytical uncertainty and decay constant.